

Comparison of Polarized Radiative Transfer Codes used by the EHT Collaboration

BEN S. PRATHER,¹ JASON DEXTER,² MONIKA MOSCIBRODZKA,³ HUNG-YI PU,^{4,5,6} THOMAS BRONZWAER,³
JORDY DAVELAAR,^{7,8,9} ZIRI YOUNSI,^{10,11} CHARLES F. GAMMIE,^{12,13,14} ROMAN GOLD¹⁵ AND GEORGE N. WONG^{16,17}

KAZUNORI AKIYAMA,^{18,19,20} ANTXON ALBERDI,²¹ WALTER ALEF,²² JUAN CARLOS ALGABA,²³
RICHARD ANANTUA,^{20,24,25} KEIICHI ASADA,⁶ REBECCA AZULAY,^{26,27,22} UWE BACH,²² ANNE-KATHRIN BACZKO,²²
DAVID BALL,²⁸ MISLAV BALOKOVIĆ,²⁹ JOHN BARRETT,¹⁸ MICHI BAUBÖCK,¹² BRADFORD A. BENSON,^{30,31}
DAN BINTLEY,^{32,33} LINDY BLACKBURN,^{20,24} RAYMOND BLUNDELL,²⁴ KATHERINE L. BOUMAN,³⁴
GEOFFREY C. BOWER,^{35,36} HOPE BOYCE,^{37,38} MICHAEL BREMER,³⁹ CHRISTIAN D. BRINKERINK,⁹
ROGER BRISSENDEN,^{20,24} SILKE BRITZEN,²² AVERY E. BRODERICK,^{40,41,42} DOMINIQUE BROGUIERE,³⁹
SANDRA BUSTAMANTE,⁴³ DO-YOUNG BYUN,^{44,45} JOHN E. CARLSTROM,^{46,31,47,48} CHIARA CECCOBELLO,⁴⁹
ANDREW CHAEL,⁵⁰ CHI-KWAN CHAN,^{28,51,52} DOMINIC O. CHANG,^{20,24} KUSHIK CHATTERJEE,^{20,24}
SHAMI CHATTERJEE,⁵³ MING-TANG CHEN,³⁵ YONGJUN CHEN (陈永军),^{54,55} XIAOPENG CHENG,⁴⁴ ILJE CHO,²¹
PIERRE CHRISTIAN,⁵⁶ NICHOLAS S. CONROY,^{13,24} JOHN E. CONWAY,⁴⁹ JAMES M. CORDES,⁵³
THOMAS M. CRAWFORD,^{31,46} GEOFFREY B. CREW,¹⁸ ALEJANDRO CRUZ-OSORIO,¹¹ YUZHU CUI (崔玉竹),^{57,58}
MARIAFELICIA DE LAURENTIS,^{59,11,60} ROGER DEANE,^{61,62,63} JESSICA DEMPSEY,^{32,33,64} GREGORY DESVIGNES,^{22,65}
VEDANT DHRUV,¹² SHEPERD S. DOELEMEN,^{20,24} SEAN DOUGAL,²⁸ SERGIO A. DZIB,^{39,22} RALPH P. EATOUGH,^{66,22}
RAZIEH EMAMI,²⁴ HEINO FALCKE,⁹ JOSEPH FARAH,^{67,68} VINCENT L. FISH,¹⁸ ED FOMALONT,⁶⁹ H. ALYSON FORD,²⁸
RAQUEL FRAGA-ENCINAS,⁹ WILLIAM T. FREEMAN,^{70,71} PER FRIBERG,^{32,33} CHRISTIAN M. FROMM,^{72,11,22}
ANTONIO FUENTES,²¹ PETER GALISON,^{20,73,74} ROBERTO GARCÍA,³⁹ OLIVIER GENTAZ,³⁹ BORIS GEORGIEV,^{41,42,40}
CIRIACO GODDI,^{75,76,77,78} ARTURO I. GÓMEZ-RUIZ,^{79,80} JOSÉ L. GÓMEZ,²¹ MINFENG GU (顾敏峰),^{54,81}
MARK GURWELL,²⁴ KAZUHIRO HADA,^{82,83} DARYL HAGGARD,^{37,38} KARI HAWORTH,²⁴ MICHAEL H. HECHT,¹⁸
RONALD HESPER,⁸⁴ DIRK HEUMANN,²⁸ LUIS C. HO (何子山),^{85,86} PAUL HO,^{6,33,32} MAREKI HONMA,^{82,83,87}
CHIH-WEI L. HUANG,⁶ LEI HUANG (黄磊),^{54,81} DAVID H. HUGHES,⁷⁹ SHIRO IKEDA,^{19,88,89,90}
C. M. VIOLETTE IMPELLIZZERI,^{91,69} MAKOTO INOUE,⁶ SARA ISSAOUN,^{24,92} DAVID J. JAMES,⁹³ BUELL T. JANNUZI,²⁸
MICHAEL JANSEN,²² BRITTON JETER,⁶ WU JIANG (江悟),⁵⁴ ALEJANDRA JIMÉNEZ-ROSALES,⁹
MICHAEL D. JOHNSON,^{20,24} SVETLANA JORSTAD,⁹⁴ ABHISHEK V. JOSHI,¹² TAEHYUN JUNG,^{44,45} MANSOUR KARAMI,^{40,41}
RAMESH KARUPPUSAMY,²² TOMOHISA KAWASHIMA,⁹⁵ GARRETT K. KEATING,²⁴ MARK KETTENIS,⁹⁶ DONG-JIN KIM,²²
JAE-YOUNG KIM,^{97,22} JONGSOO KIM,⁴⁴ JUNHAN KIM,³⁴ MOTOKI KINO,^{19,98} JUN YI KOAY,⁶
PRASHANT KOCHERLAKOTA,¹¹ YUTARO KOFUJI,^{82,87} SHOKO KOYAMA,^{99,6} CARSTEN KRAMER,³⁹ MICHAEL KRAMER,²²
THOMAS P. KRICHBAUM,²² CHENG-YU KUO,^{100,6} NOEMI LA BELLA,⁹ TOD R. LAUER,¹⁰¹ DAEYOUNG LEE,¹²
SANG-SUNG LEE,⁴⁴ PO KIN LEUNG,¹⁰² AVIAD LEVIS,³⁴ ZHIYUAN LI (李志远),^{103,104} ROCCO LICO,^{21,105}
GREG LINDAHL,²⁴ MICHAEL LINDQVIST,⁴⁹ MIKHAIL LISAKOV,²² JUN LIU (刘俊),²² KUO LIU,²² ELISABETTA LIUZZO,¹⁰⁶
WEN-PING LO,^{6,107} ANDREI P. LOBANOV,²² LAURENT LOINARD,^{108,109} COLIN J. LONSDALE,¹⁸
RU-SEN LU (路如森),^{54,55,22} NICHOLAS R. MACDONALD,²² JIRONG MAO (毛基荣),^{110,111,112} NICOLA MARCHILI,^{106,22}
SERA MARKOFF,^{113,114} DANIEL P. MARRONE,²⁸ ALAN P. MARSCHER,⁹⁴ IVÁN MARTÍ-VIDAL,^{26,27} SATOKI MATSUSHITA,⁶
LYNN D. MATTHEWS,¹⁸ LIA MEDEIROS,^{115,16,28} KARL M. MENTEN,²² DANIEL MICHALIK,^{116,31} IZUMI MIZUNO,^{32,33}
YOSUKE MIZUNO,^{58,117,11} JAMES M. MORAN,^{20,24} KOTARO MORIYAMA,^{11,18,82} CORNELIA MÜLLER,^{22,9}
ALEJANDRO MUS,^{26,27} GIBWA MUSOKE,^{113,9} IOANNIS MYSERLIS,¹¹⁸ ANDREW NADOLSKI,¹³ HIROSHI NAGAI,^{19,83}
NEIL M. NAGAR,¹¹⁹ MASANORI NAKAMURA,^{120,6} RAMESH NARAYAN,^{20,24} GOPAL NARAYANAN,⁴³
INIYAN NATARAJAN,^{24,20} ANTONIOS NATHANAIL,^{11,121} SANTIAGO NAVARRO FUENTES,¹¹⁸ JOEY NEILSEN,¹²²
ROBERTO NERI,³⁹ CHUNGHONG NI,^{41,42,40} ARISTEIDIS NOUTSOS,²² MICHAEL A. NOWAK,¹²³ JUNGHWAN OH,¹²⁴
HIROKI OKINO,^{82,87} HÉCTOR OLIVARES,⁹ GISELA N. ORTIZ-LEÓN,^{109,22} TOMOAKI OYAMA,⁸² FERYAL ÖZEL,²⁸
DANIEL C. M. PALUMBO,^{20,24} GEORGIOS FILIPPOS PARASCHOS,²² JONGHO PARK,^{44,6} HARRIET PARSONS,^{32,33}
NIMESH PATEL,²⁴ UE-LI PEN,^{6,40,125,126,127} DOMINIC W. PESCE,^{24,20} VINCENT PIÉTU,³⁹ RICHARD PLAMBECK,¹²⁸
ALEKSANDAR POPSTEFANIJA,⁴³ OLIVER PORTH,^{113,11} FELIX M. PÖTZL,^{129,22} JORGE A. PRECIADO-LÓPEZ,⁴⁰
DIMITRIOS PSALTIS,²⁸ VENKATESH RAMAKRISHNAN,^{119,130,131} RAMPRASAD RAO,²⁴ MARK G. RAWLINGS,^{132,32,33}
ALEXANDER W. RAYMOND,^{20,24} LUCIANO REZZOLLA,^{11,133,134} ANGELO RICARTE,^{24,20} BART RIPPERDA,^{16,92,135,8}
Freek ROELOFS,^{24,20,9} ALAN ROGERS,¹⁸ EDUARDO ROS,²² CRISTINA ROMERO-CAÑIZALES,⁶ ARASH ROSHANINESHAT,²⁸
HELGE ROTTMANN,²² ALAN L. ROY,²² IGNACIO RUIZ,¹¹⁸ CHET RUSZCZYK,¹⁸ KAZI L. J. RYGL,¹⁰⁶
SALVADOR SÁNCHEZ,¹¹⁸ DAVID SÁNCHEZ-ARGÜELLES,^{79,80} MIGUEL SÁNCHEZ-PORTAL,¹¹⁸ MAHITO SASADA,^{136,82,137}

KAUSHIK SATAPATHY,²⁸ TUOMAS SAVOLAINEN,^{138, 131, 22} F. PETER SCHLOERB,⁴³ JONATHAN SCHONFELD,²⁴
 KARL-FRIEDRICH SCHUSTER,³⁹ LIJING SHAO,^{86, 22} ZHIQIANG SHEN (沈志强),^{54, 55} DES SMALL,⁹⁶
 BONG WON SOHN,^{44, 45, 139} JASON SOOHOO,¹⁸ KAMAL SOUCCAR,⁴³ HE SUN (孙赫),³⁴ FUMIE TAZAKI,⁸²
 ALEXANDRA J. TETARENKO,^{140, 92} PAUL TIEDE,^{24, 20} REMO P. J. TILANUS,^{28, 9, 91, 141} MICHAEL TITUS,¹⁸
 PABLO TORNE,^{118, 22} EFTHALIA TRAIANOU,^{21, 22} TYLER TRENT,²⁸ SASCHA TRIPPE,¹⁴² MATTHEW TURK,¹³
 ILSE VAN BEMMEL,⁹⁶ HUIB JAN VAN LANGEVELDE,^{96, 91, 143} DANIEL R. VAN ROSSUM,⁹ JESSE VOS,⁹ JAN WAGNER,²²
 DEREK WARD-THOMPSON,¹⁴⁴ JOHN WARDLE,¹⁴⁵ JONATHAN WEINTROUB,^{20, 24} NORBERT WEX,²² ROBERT WHARTON,²²
 MACIEK WIELGUS,²² KAJ WIIK,¹⁴⁶ GUNTHER WITZEL,²² MICHAEL F. WONDRAK,^{9, 147} QINGWEN WU (吴庆文),¹⁴⁸
 PAUL YAMAGUCHI,²⁴ ARISTOMENIS YFANTIS,⁹ DOOSOO YOON,¹¹³ ANDRÉ YOUNG,⁹ KEN YOUNG,²⁴ WEI YU (于威),²⁴
 FENG YUAN (袁峰),^{54, 81, 149} YE-FEI YUAN (袁业飞),¹⁵⁰ J. ANTON ZENSUS,²² SHUO ZHANG,¹⁵¹ GUANG-YAO ZHAO,²¹
 SHAN-SHAN ZHAO (赵杉杉),⁵⁴

THE EVENT HORIZON TELESCOPE COLLABORATION

¹*CCS-2, Los Alamos National Laboratory, P.O. Box 1663, Los Alamos, NM 87545, USA*

²*JILA and Department of Astrophysical and Planetary Sciences, University of Colorado, Boulder, CO 80309, USA*

³*Department of Astrophysics/IMAPP, Radboud University, P.O. Box 9010, 6500 GL Nijmegen, The Netherlands*

⁴*Department of Physics, National Taiwan Normal University, No. 88, Sec.4, Tingzhou Rd., Taipei 116, Taiwan, R.O.C.*

⁵*Center of Astronomy and Gravitation, National Taiwan Normal University, No. 88, Sec. 4, Tingzhou Road, Taipei 116, Taiwan, R.O.C.*

⁶*Institute of Astronomy and Astrophysics, Academia Sinica, 11F of Astronomy-Mathematics Building, AS/NTU No. 1, Sec. 4, Roosevelt Rd, Taipei 10617, Taiwan, R.O.C.*

⁷*Department of Astronomy and Columbia Astrophysics Laboratory, Columbia University, 550 W 120th Street, New York, NY 10027, USA*

⁸*Center for Computational Astrophysics, Flatiron Institute, 162 Fifth Avenue, New York, NY 10010, USA*

⁹*Department of Astrophysics, Institute for Mathematics, Astrophysics and Particle Physics (IMAPP), Radboud University, P.O. Box 9010, 6500 GL Nijmegen, The Netherlands*

¹⁰*Mullard Space Science Laboratory, University College London, Holmbury St. Mary, Dorking, Surrey, RH5 6NT, UK*

¹¹*Institut für Theoretische Physik, Goethe-Universität Frankfurt, Max-von-Laue-Straße 1, D-60438 Frankfurt am Main, Germany*

¹²*Department of Physics, University of Illinois, 1110 West Green Street, Urbana, IL 61801, USA*

¹³*Department of Astronomy, University of Illinois at Urbana-Champaign, 1002 West Green Street, Urbana, IL 61801, USA*

¹⁴*NCSA, University of Illinois, 1205 W Clark St, Urbana, IL 61801, USA*

¹⁵*CP3-Origins, University of Southern Denmark, Campusvej 55, DK-5230 Odense M, Denmark*

¹⁶*School of Natural Sciences, Institute for Advanced Study, 1 Einstein Drive, Princeton, NJ 08540, USA*

¹⁷*Princeton Gravity Initiative, Princeton University, Princeton, New Jersey 08544, USA*

¹⁸*Massachusetts Institute of Technology Haystack Observatory, 99 Millstone Road, Westford, MA 01886, USA*

¹⁹*National Astronomical Observatory of Japan, 2-21-1 Osawa, Mitaka, Tokyo 181-8588, Japan*

²⁰*Black Hole Initiative at Harvard University, 20 Garden Street, Cambridge, MA 02138, USA*

²¹*Instituto de Astrofísica de Andalucía-CSIC, Glorieta de la Astronomía s/n, E-18008 Granada, Spain*

²²*Max-Planck-Institut für Radioastronomie, Auf dem Hügel 69, D-53121 Bonn, Germany*

²³*Department of Physics, Faculty of Science, Universiti Malaya, 50603 Kuala Lumpur, Malaysia*

²⁴*Center for Astrophysics | Harvard & Smithsonian, 60 Garden Street, Cambridge, MA 02138, USA*

²⁵*Department of Physics & Astronomy, The University of Texas at San Antonio, One UTSA Circle, San Antonio, TX 78249, USA*

²⁶*Departament d'Astronomia i Astrofísica, Universitat de València, C. Dr. Moliner 50, E-46100 Burjassot, València, Spain*

²⁷*Observatori Astronòmic, Universitat de València, C. Catedrático José Beltrán 2, E-46980 Paterna, València, Spain*

²⁸*Steward Observatory and Department of Astronomy, University of Arizona, 933 N. Cherry Ave., Tucson, AZ 85721, USA*

²⁹*Yale Center for Astronomy & Astrophysics, Yale University, 52 Hillhouse Avenue, New Haven, CT 06511, USA*

³⁰*Fermi National Accelerator Laboratory, MS209, P.O. Box 500, Batavia, IL 60510, USA*

³¹*Department of Astronomy and Astrophysics, University of Chicago, 5640 South Ellis Avenue, Chicago, IL 60637, USA*

³²*East Asian Observatory, 660 N. A'ohoku Place, Hilo, HI 96720, USA*

³³*James Clerk Maxwell Telescope (JCMT), 660 N. A'ohoku Place, Hilo, HI 96720, USA*

³⁴*California Institute of Technology, 1200 East California Boulevard, Pasadena, CA 91125, USA*

³⁵*Institute of Astronomy and Astrophysics, Academia Sinica, 645 N. A'ohoku Place, Hilo, HI 96720, USA*

³⁶*Department of Physics and Astronomy, University of Hawaii at Manoa, 2505 Correa Road, Honolulu, HI 96822, USA*

³⁷*Department of Physics, McGill University, 3600 rue University, Montréal, QC H3A 2T8, Canada*

³⁸*McGill Space Institute, McGill University, 3550 rue University, Montréal, QC H3A 2A7, Canada*

³⁹*Institut de Radioastronomie Millimétrique (IRAM), 300 rue de la Piscine, F-38406 Saint Martin d'Hères, France*

⁴⁰*Perimeter Institute for Theoretical Physics, 31 Caroline Street North, Waterloo, ON, N2L 2Y5, Canada*

⁴¹*Department of Physics and Astronomy, University of Waterloo, 200 University Avenue West, Waterloo, ON, N2L 3G1, Canada*

- ⁴² *Waterloo Centre for Astrophysics, University of Waterloo, Waterloo, ON, N2L 3G1, Canada*
- ⁴³ *Department of Astronomy, University of Massachusetts, 01003, Amherst, MA, USA*
- ⁴⁴ *Korea Astronomy and Space Science Institute, Daedeok-daero 776, Yuseong-gu, Daejeon 34055, Republic of Korea*
- ⁴⁵ *University of Science and Technology, Gajeong-ro 217, Yuseong-gu, Daejeon 34113, Republic of Korea*
- ⁴⁶ *Kavli Institute for Cosmological Physics, University of Chicago, 5640 South Ellis Avenue, Chicago, IL 60637, USA*
- ⁴⁷ *Department of Physics, University of Chicago, 5720 South Ellis Avenue, Chicago, IL 60637, USA*
- ⁴⁸ *Enrico Fermi Institute, University of Chicago, 5640 South Ellis Avenue, Chicago, IL 60637, USA*
- ⁴⁹ *Department of Space, Earth and Environment, Chalmers University of Technology, Onsala Space Observatory, SE-43992 Onsala, Sweden*
- ⁵⁰ *Princeton Gravity Initiative, Jadwin Hall, Princeton University, Princeton, NJ 08544, USA*
- ⁵¹ *Data Science Institute, University of Arizona, 1230 N. Cherry Ave., Tucson, AZ 85721, USA*
- ⁵² *Program in Applied Mathematics, University of Arizona, 617 N. Santa Rita, Tucson, AZ 85721*
- ⁵³ *Cornell Center for Astrophysics and Planetary Science, Cornell University, Ithaca, NY 14853, USA*
- ⁵⁴ *Shanghai Astronomical Observatory, Chinese Academy of Sciences, 80 Nandan Road, Shanghai 200030, People's Republic of China*
- ⁵⁵ *Key Laboratory of Radio Astronomy, Chinese Academy of Sciences, Nanjing 210008, People's Republic of China*
- ⁵⁶ *Physics Department, Fairfield University, 1073 North Benson Road, Fairfield, CT 06824, USA*
- ⁵⁷ *Research Center for Intelligent Computing Platforms, Zhejiang Laboratory, Hangzhou 311100, China*
- ⁵⁸ *Tsung-Dao Lee Institute, Shanghai Jiao Tong University, Shengrong Road 520, Shanghai, 201210, People's Republic of China*
- ⁵⁹ *Dipartimento di Fisica "E. Pancini", Università di Napoli "Federico II", Compl. Univ. di Monte S. Angelo, Edificio G, Via Cinthia, I-80126, Napoli, Italy*
- ⁶⁰ *INFN Sez. di Napoli, Compl. Univ. di Monte S. Angelo, Edificio G, Via Cinthia, I-80126, Napoli, Italy*
- ⁶¹ *Wits Centre for Astrophysics, University of the Witwatersrand, 1 Jan Smuts Avenue, Braamfontein, Johannesburg 2050, South Africa*
- ⁶² *Department of Physics, University of Pretoria, Hatfield, Pretoria 0028, South Africa*
- ⁶³ *Centre for Radio Astronomy Techniques and Technologies, Department of Physics and Electronics, Rhodes University, Makhanda 6140, South Africa*
- ⁶⁴ *ASTRON, Oude Hoogeveensedijk 4, 7991 PD Dwingeloo, The Netherlands*
- ⁶⁵ *LESIA, Observatoire de Paris, Université PSL, CNRS, Sorbonne Université, Université de Paris, 5 place Jules Janssen, 92195 Meudon, France*
- ⁶⁶ *National Astronomical Observatories, Chinese Academy of Sciences, 20A Datun Road, Chaoyang District, Beijing 100101, PR China*
- ⁶⁷ *Las Cumbres Observatory, 6740 Cortona Drive, Suite 102, Goleta, CA 93117-5575, USA*
- ⁶⁸ *Department of Physics, University of California, Santa Barbara, CA 93106-9530, USA*
- ⁶⁹ *National Radio Astronomy Observatory, 520 Edgemont Road, Charlottesville, VA 22903, USA*
- ⁷⁰ *Department of Electrical Engineering and Computer Science, Massachusetts Institute of Technology, 32-D476, 77 Massachusetts Ave., Cambridge, MA 02142, USA*
- ⁷¹ *Google Research, 355 Main St., Cambridge, MA 02142, USA*
- ⁷² *Institut für Theoretische Physik und Astrophysik, Universität Würzburg, Emil-Fischer-Str. 31, 97074 Würzburg, Germany*
- ⁷³ *Department of History of Science, Harvard University, Cambridge, MA 02138, USA*
- ⁷⁴ *Department of Physics, Harvard University, Cambridge, MA 02138, USA*
- ⁷⁵ *Universidade de Sao Paulo, Instituto de Astronomia, Geofísica e Ciências Atmosféricas, Departamento de Astronomia, Sao Paulo, SP 05508-090, Brazil*
- ⁷⁶ *Dipartimento di Fisica, Università degli Studi di Cagliari, SP Monserrato-Sestu km 0.7, I-09042 Monserrato, Italy*
- ⁷⁷ *INAF - Osservatorio Astronomico di Cagliari, Via della Scienza 5, 09047, Selargius, CA, Italy*
- ⁷⁸ *INFN, Sezione di Cagliari, Cittadella Univ., I-09042 Monserrato (CA), Italy*
- ⁷⁹ *Instituto Nacional de Astrofísica, Óptica y Electrónica. Apartado Postal 51 y 216, 72000. Puebla Pue., México*
- ⁸⁰ *Consejo Nacional de Ciencia y Tecnología, Av. Insurgentes Sur 1582, 03940, Ciudad de México, México*
- ⁸¹ *Key Laboratory for Research in Galaxies and Cosmology, Chinese Academy of Sciences, Shanghai 200030, People's Republic of China*
- ⁸² *Mizusawa VLBI Observatory, National Astronomical Observatory of Japan, 2-12 Hoshigaoka, Mizusawa, Oshu, Iwate 023-0861, Japan*
- ⁸³ *Department of Astronomical Science, The Graduate University for Advanced Studies (SOKENDAI), 2-21-1 Osawa, Mitaka, Tokyo 181-8588, Japan*
- ⁸⁴ *NOVA Sub-mm Instrumentation Group, Kapteyn Astronomical Institute, University of Groningen, Landleven 12, 9747 AD Groningen, The Netherlands*
- ⁸⁵ *Department of Astronomy, School of Physics, Peking University, Beijing 100871, People's Republic of China*
- ⁸⁶ *Kavli Institute for Astronomy and Astrophysics, Peking University, Beijing 100871, People's Republic of China*
- ⁸⁷ *Department of Astronomy, Graduate School of Science, The University of Tokyo, 7-3-1 Hongo, Bunkyo-ku, Tokyo 113-0033, Japan*
- ⁸⁸ *The Institute of Statistical Mathematics, 10-3 Midori-cho, Tachikawa, Tokyo, 190-8562, Japan*
- ⁸⁹ *Department of Statistical Science, The Graduate University for Advanced Studies (SOKENDAI), 10-3 Midori-cho, Tachikawa, Tokyo 190-8562, Japan*

- ⁹⁰*Kavli Institute for the Physics and Mathematics of the Universe, The University of Tokyo, 5-1-5 Kashiwanoha, Kashiwa, 277-8583, Japan*
- ⁹¹*Leiden Observatory, Leiden University, Postbus 2300, 9513 RA Leiden, The Netherlands*
- ⁹²*NASA Hubble Fellowship Program, Einstein Fellow*
- ⁹³*ASTRAVEO LLC, PO Box 1668, Gloucester, MA 01931*
- ⁹⁴*Institute for Astrophysical Research, Boston University, 725 Commonwealth Ave., Boston, MA 02215, USA*
- ⁹⁵*Institute for Cosmic Ray Research, The University of Tokyo, 5-1-5 Kashiwanoha, Kashiwa, Chiba 277-8582, Japan*
- ⁹⁶*Joint Institute for VLBI ERIC (JIVE), Oude Hoogeveensedijk 4, 7991 PD Dwingeloo, The Netherlands*
- ⁹⁷*Department of Astronomy and Atmospheric Sciences, Kyungpook National University, Daegu 702-701, Republic of Korea*
- ⁹⁸*Kogakuin University of Technology & Engineering, Academic Support Center, 2665-1 Nakano, Hachioji, Tokyo 192-0015, Japan*
- ⁹⁹*Niigata University, 8050 Ikarashi-nino-cho, Nishi-ku, Niigata 950-2181, Japan*
- ¹⁰⁰*Physics Department, National Sun Yat-Sen University, No. 70, Lien-Hai Road, Kaosiung City 80424, Taiwan, R.O.C.*
- ¹⁰¹*National Optical Astronomy Observatory, 950 N. Cherry Ave., Tucson, AZ 85719, USA*
- ¹⁰²*Department of Physics, The Chinese University of Hong Kong, Shatin, N. T., Hong Kong*
- ¹⁰³*School of Astronomy and Space Science, Nanjing University, Nanjing 210023, People's Republic of China*
- ¹⁰⁴*Key Laboratory of Modern Astronomy and Astrophysics, Nanjing University, Nanjing 210023, People's Republic of China*
- ¹⁰⁵*INAF-Istituto di Radioastronomia, Via P. Gobetti 101, I-40129 Bologna, Italy*
- ¹⁰⁶*INAF-Istituto di Radioastronomia & Italian ALMA Regional Centre, Via P. Gobetti 101, I-40129 Bologna, Italy*
- ¹⁰⁷*Department of Physics, National Taiwan University, No.1, Sect.4, Roosevelt Rd., Taipei 10617, Taiwan, R.O.C*
- ¹⁰⁸*Instituto de Radioastronomía y Astrofísica, Universidad Nacional Autónoma de México, Morelia 58089, México*
- ¹⁰⁹*Instituto de Astronomía, Universidad Nacional Autónoma de México (UNAM), Apdo Postal 70-264, Ciudad de México, México*
- ¹¹⁰*Yunnan Observatories, Chinese Academy of Sciences, 650011 Kunming, Yunnan Province, People's Republic of China*
- ¹¹¹*Center for Astronomical Mega-Science, Chinese Academy of Sciences, 20A Datun Road, Chaoyang District, Beijing, 100012, People's Republic of China*
- ¹¹²*Key Laboratory for the Structure and Evolution of Celestial Objects, Chinese Academy of Sciences, 650011 Kunming, People's Republic of China*
- ¹¹³*Anton Pannekoek Institute for Astronomy, University of Amsterdam, Science Park 904, 1098 XH, Amsterdam, The Netherlands*
- ¹¹⁴*Gravitation and Astroparticle Physics Amsterdam (GRAPPA) Institute, University of Amsterdam, Science Park 904, 1098 XH Amsterdam, The Netherlands*
- ¹¹⁵*NSF Astronomy and Astrophysics Postdoctoral Fellow*
- ¹¹⁶*Science Support Office, Directorate of Science, European Space Research and Technology Centre (ESA/ESTEC), Keplerlaan 1, 2201 AZ Noordwijk, The Netherlands*
- ¹¹⁷*School of Physics and Astronomy, Shanghai Jiao Tong University, 800 Dongchuan Road, Shanghai, 200240, People's Republic of China*
- ¹¹⁸*Institut de Radioastronomie Millimétrique (IRAM), Avenida Divina Pastora 7, Local 20, E-18012, Granada, Spain*
- ¹¹⁹*Astronomy Department, Universidad de Concepción, Casilla 160-C, Concepción, Chile*
- ¹²⁰*National Institute of Technology, Hachinohe College, 16-1 Uwanotai, Tamonoki, Hachinohe City, Aomori 039-1192, Japan*
- ¹²¹*Department of Physics, National and Kapodistrian University of Athens, Panepistimiopolis, GR 15783 Zografos, Greece*
- ¹²²*Department of Physics, Villanova University, 800 Lancaster Avenue, Villanova, PA 19085, USA*
- ¹²³*Physics Department, Washington University CB 1105, St Louis, MO 63130, USA*
- ¹²⁴*Sejong University, 209 Neungdong-ro, Gwangjin-gu, Seoul, Republic of Korea*
- ¹²⁵*Canadian Institute for Theoretical Astrophysics, University of Toronto, 60 St. George Street, Toronto, ON, M5S 3H8, Canada*
- ¹²⁶*Dunlap Institute for Astronomy and Astrophysics, University of Toronto, 50 St. George Street, Toronto, ON, M5S 3H4, Canada*
- ¹²⁷*Canadian Institute for Advanced Research, 180 Dundas St West, Toronto, ON, M5G 1Z8, Canada*
- ¹²⁸*Radio Astronomy Laboratory, University of California, Berkeley, CA 94720, USA*
- ¹²⁹*Institute of Astrophysics, Foundation for Research and Technology - Hellas, Voutes, 7110 Heraklion, Greece*
- ¹³⁰*Finnish Centre for Astronomy with ESO, FI-20014 University of Turku, Finland*
- ¹³¹*Aalto University Metsähovi Radio Observatory, Metsähovintie 114, FI-02540 Kylmälä, Finland*
- ¹³²*Gemini Observatory/NSF NOIRLab, 670 N. A'ohōkū Place, Hilo, HI 96720, USA*
- ¹³³*Frankfurt Institute for Advanced Studies, Ruth-Moufang-Strasse 1, 60438 Frankfurt, Germany*
- ¹³⁴*School of Mathematics, Trinity College, Dublin 2, Ireland*
- ¹³⁵*Department of Astrophysical Sciences, Peyton Hall, Princeton University, Princeton, NJ 08544, USA*
- ¹³⁶*Department of Physics, Tokyo Institute of Technology, 2-12-1 Ookayama, Meguro-ku, Tokyo 152-8551, Japan*
- ¹³⁷*Hiroshima Astrophysical Science Center, Hiroshima University, 1-3-1 Kagamiyama, Higashi-Hiroshima, Hiroshima 739-8526, Japan*
- ¹³⁸*Aalto University Department of Electronics and Nanoengineering, PL 15500, FI-00076 Aalto, Finland*
- ¹³⁹*Department of Astronomy, Yonsei University, Yonsei-ro 50, Seodaemun-gu, 03722 Seoul, Republic of Korea*
- ¹⁴⁰*Department of Physics and Astronomy, Texas Tech University, Lubbock, Texas 79409-1051, USA*
- ¹⁴¹*Netherlands Organisation for Scientific Research (NWO), Postbus 93138, 2509 AC Den Haag, The Netherlands*

¹⁴²*Department of Physics and Astronomy, Seoul National University, Gwanak-gu, Seoul 08826, Republic of Korea*

¹⁴³*University of New Mexico, Department of Physics and Astronomy, Albuquerque, NM 87131, USA*

¹⁴⁴*Jeremiah Horrocks Institute, University of Central Lancashire, Preston PR1 2HE, UK*

¹⁴⁵*Physics Department, Brandeis University, 415 South Street, Waltham, MA 02453, USA*

¹⁴⁶*Tuorla Observatory, Department of Physics and Astronomy, University of Turku, Finland*

¹⁴⁷*Radboud Excellence Fellow of Radboud University, Nijmegen, The Netherlands*

¹⁴⁸*School of Physics, Huazhong University of Science and Technology, Wuhan, Hubei, 430074, People's Republic of China*

¹⁴⁹*School of Astronomy and Space Sciences, University of Chinese Academy of Sciences, No. 19A Yuquan Road, Beijing 100049, People's Republic of China*

¹⁵⁰*Astronomy Department, University of Science and Technology of China, Hefei 230026, People's Republic of China*

¹⁵¹*Bard College, 30 Campus Road, Annandale-on-Hudson, NY, 12504*

(Dated: March 22, 2023)

ABSTRACT

Interpretation of resolved polarized images of black holes by the Event Horizon Telescope (EHT) requires predictions of the polarized emission observable by an Earth-based instrument for a particular model of the black hole accretion system. Such predictions are generated by general relativistic radiative transfer (GRRT) codes, which integrate the equations of polarized radiative transfer in curved spacetime. A selection of ray-tracing GRRT codes used within the EHT collaboration is evaluated for accuracy and consistency in producing a selection of test images, demonstrating that the various methods and implementations of radiative transfer calculations are highly consistent. When imaging an analytic accretion model, we find that all codes produce images similar within a pixel-wise normalized mean squared error (NMSE) of 0.012 in the worst case. When imaging a snapshot from a cell-based magnetohydrodynamic simulation, we find all test images to be similar within NMSEs of 0.02, 0.04, 0.04, and 0.12 in Stokes I , Q , U , and V respectively. We additionally find the values of several image metrics relevant to published EHT results to be in agreement to much better precision than measurement uncertainties.

1. INTRODUCTION

In 2019, the Event Horizon Telescope (EHT) collaboration published images of the central black hole in the galaxy M87 (hereafter M87*), which measured and interpreted the total intensity of radio emission in two bands near 230 GHz (Event Horizon Telescope Collaboration et al. 2019a,b,c,d,e,f, hereafter EHTC I; EHTC II; EHTC III; EHTC IV; EHTC V; EHTC VI). In 2021, additional results were released measuring the degree and distribution of linear polarization across the image of M87*, measured via the Stokes parameters Q and U (Event Horizon Telescope Collaboration et al. 2021a,b, hereafter EHTC VII; EHTC VIII). Linear polarization results are also expected of the central-Milky Way black hole Sgr A* accompanying total-intensity results published in 2022 (Event Horizon Telescope Collaboration et al. 2022a,b,c,d,e,f).

In order to interpret polarized observations, the collaboration generated models of the accreting plasma around M87*, usually with general relativistic magnetohydrodynamic (GRMHD) simulations. Simulated images were generated from the models via general relativistic radiative transfer (GRRT) calculations in order to predict the emission visible from earth from the gener-

ated plasma state (EHTC V, see also Wong et al. 2022). The total-intensity images produced by various GRRT codes were validated against analytically-defined tests in Gold et al. (2020) and found to be in good agreement. That paper also compared the output of certain pairs of codes, but not all codes, when imaging GRMHD simulation data.

The interpretation of the linear-polarimetric EHT image, performed in Event Horizon Telescope Collaboration et al. 2021b (hereafter EHTC VIII), also used synthetic images. Polarimetric images are more complicated than total-intensity images as they predict the linear and circular polarization parameters (Stokes Q , U , V) in addition to the total intensity (Stokes I). Predicting polarized emission involves solving the coupled polarized radiative transfer equations, which can introduce significant additional computational problems, such as the treatment of rapid Faraday rotation and the need to parallel transport the linear polarization direction through curved spacetime. The additional complexity merits a separate comparison of polarized radiative transfer schemes present in several of the codes compared in Gold et al. (2020). That comparison is presented in this paper.

This paper provides brief descriptions of the codes compared, specifications of the tests performed, and measurements of code error (where available) or similarity as a group, compared against parameter changes and estimated detector accuracy.

The paper is structured as follows. In Section 2 we briefly describe all codes participating in the comparison study. In section 3 we define three test problems used to compare the codes. In section 4 we define metric to evaluate light-curves and image similarities and we present the results of the comparisons. The discussion of the results and limitations of the examined ray-tracing radiative transfer schemes are given in section 5. We conclude our study in section 6.

2. PARTICIPATING CODES

2.1. BHOSS

The BHOSS code (Younsi et al. 2012, 2020) numerically integrates, for an arbitrary input spacetime metric tensor, the geodesic equations of motion coupled with the covariant polarized radiative transfer equations. The solution of the polarized radiative transfer equations is achieved via parallel-propagation of a pair of mutually-orthogonal basis 4-vectors which define the observer’s frame. A fourth-order Runge-Kutta-Fehlberg method with 5th order error estimate and adaptive stepsize control, hereafter RKF4(5), is typically used. In regions of higher Faraday depth, a RKF8(9) method is used, and when the transfer equations are particularly stiff a variable-order implicit RKF integrator is employed.

2.2. ipole

The ipole code¹ (Mościbrodzka & Gammie 2018, Noble et al. 2007) is a publicly available ray-tracing scheme for covariant polarized GRRT. ipole splits the radiative transfer problem into two steps. In the fluid frame it evolves the Stokes parameters taking into account synchrotron emission, absorption and Faraday effects and using an analytic solution to the polarized transfer equations with constant coefficients. Currently two analytic solvers are implemented in the code (Landi Degl’Innocenti & Landi Degl’Innocenti 1985 and the one presented in the Appendix A of Mościbrodzka & Gammie 2018). Analytic solvers make ipole solutions numerically stable even for plasma with large optical or Faraday depths. In the coordinate frame, the parallel transport of the Stokes parameters is accomplished by transport of coherency matrix rather than Stokes

parameters themselves. Hence ipole radiative transfer is coordinate and metric independent. ipole has been tested against another polarized ray-tracing code grtrans (see method paper Mościbrodzka & Gammie 2018 and the next subsection) and against a polarized Monte Carlo radiative transfer scheme (see Mościbrodzka 2020 and Appendix A of this work). ipole was used in EHTC VIII for calculating polarized images of models with accelerated electrons.

2.3. ipole-IL

ipole-IL², usually also called ipole but suffixed in this comparison for clarity, is a fork of the original ipole code described above, with features designed for treating libraries of GRMHD snapshot files, particularly from iharm3D as a part of the PATOKA pipeline (Wong et al. 2022). It maintains the same transport scheme implemented in ipole, but adds robustness features such as reorthogonalization of tetrad basis vectors and additional limiting cases for the analytic solutions and fits. It also adds compatibility with a number of different GRMHD codes and supports calculating emission from different electron energy distribution functions.

2.4. grtrans

The grtrans code³ (Dexter & Agol 2009; Dexter 2016) solves the polarized radiative transfer equations along null geodesics in a Kerr spacetime. The radiative transfer equations are integrated either numerically (Hindmarsh 2019) or with quadrature methods (Landi Degl’Innocenti & Landi Degl’Innocenti 1985; Rees et al. 1989). The quadrature methods are the most accurate and efficient for calculations of polarized radiative transfer in Faraday thick problems and are used for the test problems discussed here.

2.5. Odyssey

The Odyssey code (Pu et al. 2016) is a public GPU-based code⁴ which solves the unpolarized radiative transfer equation along null geodesics from the observer to the source (observer-to-source) in Kerr spacetime. In Pu & Broderick (2018), to implement the polarization computations and fit the need for solving the Stokes parameters along the null geodesic from the source to the observer (source-to-observer), a two stage scheme is proposed: (i) during the observer-to-source stage, unpolarized radiative transfer is computed backward in time, (ii) inverse the time direction and trace the same

¹ Current version is available at <https://github.com/moscibrodzka/ipole>

² <https://github.com/AFD-Illinois/ipole>

³ <https://github.com/jadexter/grtrans>

⁴ <https://github.com/hungyipu/Odyssey>

geodesic during source-to-observer stage, and simultaneously solve the four Stokes parameters. As a result, there are four additional ODEs (related to the Stokes parameters) to be solved in the second stage compared to that in the first stage. By controlling the time direction directly in the code, there is no need to save the photon path during the observer-to-source stage for the use of source-to-observer stage. However, the caveat is that the cost for solving additional four Stokes parameters during the source-to-observer stage can be computationally costly, and the Runge-Kutta scheme may fail when complicated Faraday coefficients are introduced in a given problem.

In this work, to improve its speed and the stability, we improve the polarization scheme of *Odyssey* with the following: (i) a two stage scheme is still adopted, without solving the four ODEs for Stokes parameters during the second (source-to-observer) stage. (ii) Instead, during the second stage, the Stokes parameters are solved along the geodesics with an implicit method (Bronzwaer et al. 2020; Pihajoki et al. 2018). In this new scheme, the accuracy of the polarization computation is automatically controlled by the accuracy of the geodesic computation. The modifications significantly improve the computational speed. For example, it takes about a second (including the time for reading GRMHD simulation data) for *Odyssey* to finish the computation for the GRMHD snapshot test problem (§3.3).

2.6. RAPTOR

The **RAPTOR** code (Bronzwaer et al. 2018, 2020)⁵ is a public code that numerically integrates the equations of motion of light rays in arbitrary spacetimes and then performs polarized radiative transfer calculations along the rays. The code uses an adaptive Runge-Kutta-Fehlberg scheme to integrate the geodesic equation where the Christoffel symbols can either be provided analytically or are numerically computed on the fly by using a fourth order centered finite difference method. To integrate the polarized radiative transfer equation **RAPTOR** uses a hybrid ImEx integration scheme that switches to an implicit integrator in case of stiffness, in order to solve the equation with optimal speed and accuracy for all possible values of the local optical/Faraday thickness of the plasma. The code uses an adaptive camera grid to optimize run time by adding resolution where needed (Davelaar & Haiman 2022), and can produce virtual reality visualizations (Davelaar et al. 2018). The code is fully interfaced with the non-uniform

grid (adaptive mesh refinement) data format of the **BHAC** code (Davelaar et al. 2019). Radiative transfer coefficients are provided for the thermal electron distribution, but also the κ and power-law distributions.

3. TEST PROBLEMS

Three test problems were used to evaluate the codes. The problems were chosen to reflect tests already present in the literature, highlighting specifically the aspects of code performance related to polarized transport. A previous comparison (Gold et al. 2020) evaluated many of the same codes for similarity and accuracy in producing total-intensity images. An additional goal was to verify data product similarity when imaging the output of GRMHD simulations, a test evaluated only for certain pairs of codes considered in Gold et al. (2020). The tests are described here from least to most complex, with each testing a larger subset of code features.

3.1. Comparison to Analytic Result

The first test problem is a straightforward integration of the non-relativistic polarized transfer equation using constant coefficients, chosen for the availability of an analytic solution from Landi Degl’Innocenti & Landi Degl’Innocenti (1985), allowing direct evaluation of code accuracy, in addition to code similarity. The test here is taken directly from Dexter (2016), with coefficients as listed in Mościbrodzka & Gammie (2018).

In the Stokes basis I, Q, U, V , the non-relativistic polarized radiative transfer equation is

$$\frac{d}{ds} \begin{pmatrix} I \\ Q \\ U \\ V \end{pmatrix} = \begin{pmatrix} j_I \\ j_Q \\ j_U \\ j_V \end{pmatrix} - \begin{pmatrix} \alpha_I & \alpha_Q & \alpha_U & \alpha_V \\ \alpha_Q & \alpha_I & \rho_V & -\rho_U \\ \alpha_U & -\rho_V & \alpha_I & \rho_Q \\ \alpha_V & \rho_U & -\rho_Q & \alpha_I \end{pmatrix} \begin{pmatrix} I \\ Q \\ U \\ V \end{pmatrix}. \quad (1)$$

In the test, this equation is integrated twice with different subsets of coefficients nonzero. This minimizes the complexity of the analytic comparison functions, isolating any bugs in treating emission and absorption from those in Faraday rotation and conversion. The coefficients for each integration are given in Table 1.

3.2. Thin-Disk Model

The second test problem consists of imaging emission from a thin opaque disk aligned to the midplane of a near-maximally spinning black hole, as described in Novikov & Thorne (1973). This involves solving the geodesic equation in two contexts: first in tracing lines of sight from the camera through the Kerr metric and

⁵ <https://github.com/jordydavelaar/raptor>

	j_I	j_Q	j_U	j_V	α_I	α_Q	α_U	α_V	ρ_Q	ρ_U	ρ_V
Emission/Absorption	2.0	1.0	0.0	0.0	1.0	1.2	0.0	0.0	0.0	0.0	0.0
Rotation	0.0	0.1	0.1	0.1	0.0	0.0	0.0	0.0	10.0	0.0	-4.0

Table 1. Constant coefficients for the analytic comparison test integrations – these mirror values in Mościbrodzka & Gammie (2018). See Section 3.1.

second in parallel-transporting the direction of linearly polarized emission from the disk back to the camera. This test closely mirrors a figure from Schnittman & Krolik (2009), which is reproduced as a test in Dexter (2016).

The thin-disk test does not include any diffuse emission: that is, all transport coefficients $j_S, \alpha_S, \rho_S = 0$ uniformly for all Stokes parameters S . Instead, the initial Stokes parameters are set as a boundary condition at the first midplane crossing of each geodesic when traced backward from the camera. As in Schnittman & Krolik (2009), the total flux F is taken from Page & Thorne (1974), and the intensity at the desired frequency I_ν is obtained by calculating an effective temperature and assuming a black-body distribution diluted by a hardening factor $n = 1.8$:

$$T_{\text{eff}} \equiv \left(\frac{F}{\sigma} \right)^{1/4}, \quad (2)$$

$$I_\nu = \frac{1}{n^4} B_\nu(n \cdot T_{\text{eff}}), \quad (3)$$

where F is the total emitted power per area of the thin disk, and $B_\nu(T)$ is the black-body function of the temperature T and the emitted frequency ν in the fluid frame.

The emitted intensity and horizontal polarization fraction in the outgoing direction are determined by assuming scattering from a semi-infinite atmosphere, as in Chandrasekhar (1960), Table 24, with the direction of linear polarization pointing along the plane of the disk. Emission is enabled only between r_{ISCO} and $R_{\text{out}} = 100r_g$, where r_g is the system gravitational radius GM_{BH}/c^2 with G the gravitational constant and c the speed of light. The fluid orbital angular velocity u^ϕ/u^t is assumed to be Keplerian:

$$\frac{u^\phi}{u^t} = \frac{1}{r^{3/2} + a_*}. \quad (4)$$

where a_* is the dimensionless form of the BH angular momentum J , $a_* \equiv Jc/GM^2$ with $-1 \leq a_* \leq 1$. As the test will need to be implemented in many different codes, we simplify the original problem from Schnittman & Krolik (2009) by observing at only a single frequency

rather than summing over a range. The full set of parameters used for this image is:

$$a_* = 0.99 \quad (5a)$$

$$M_{\text{BH}} = 10 M_\odot = 1.477 \cdot 10^6 \text{cm} \frac{c^2}{G} \quad (5b)$$

$$D_{\text{source}} = 0.05 \text{ pc} \quad (5c)$$

$$\dot{M} = 0.1 \dot{M}_{\text{Edd}} \approx 2.218 \cdot 10^{-9} M_\odot/\text{yr} \quad (5d)$$

$$h\nu = 1 \text{keV} \quad (5e)$$

where these parameters define observation at a single frequency ν of a BH of mass M_{BH} at distance D_{source} , characterized by a Kerr spacetime with BH spin parameter a_* , and accreting at rate \dot{M} . Following Dexter and Schnittman, $\dot{M}_{\text{Edd}} \equiv L_{\text{Edd}}/c^2$.

Example output from this test run with ipole-IL is shown in Figure 1. As no circularly polarized emission or Faraday conversion occurs in the problem, the Stokes V flux remains exactly zero.

3.2.1. Camera

In this and the following test, the camera tetrad is constructed such that a geodesic at the center of the camera’s field of view (FOV) would have zero angular momentum k_ϕ . The polar angle θ_{cam} is defined relative to the BH angular momentum vector. This is identical to the camera definition from Gold et al. (2020).

The camera is placed at radius $10^4 r_g$ in both tests, to reduce the discrepancy between pinhole and planar cameras. Note that R_{cam} is in this case and in practice much smaller than D_{source} – so long as R_{cam} is large enough to eliminate camera effects, the image intensity is invariant with distance.

The FOV of each test is given in two forms: DX, the in-plane distance from one edge of the imaged material to the other in gravitational radii r_g , and FOV, the angular size from Earth in micro-arcseconds (μas).

Pixels on each image correspond to evenly spaced geodesics, starting from each pixel center. That is, an image with a FOV of $80 \mu\text{as}$ to a side and NX of 80 pixels would be calculated using geodesics originating at $-39.5 \mu\text{as}$ to $39.5 \mu\text{as}$ away from the FOV center, spaced $1 \mu\text{as}$ apart in each cardinal direction. All images in these

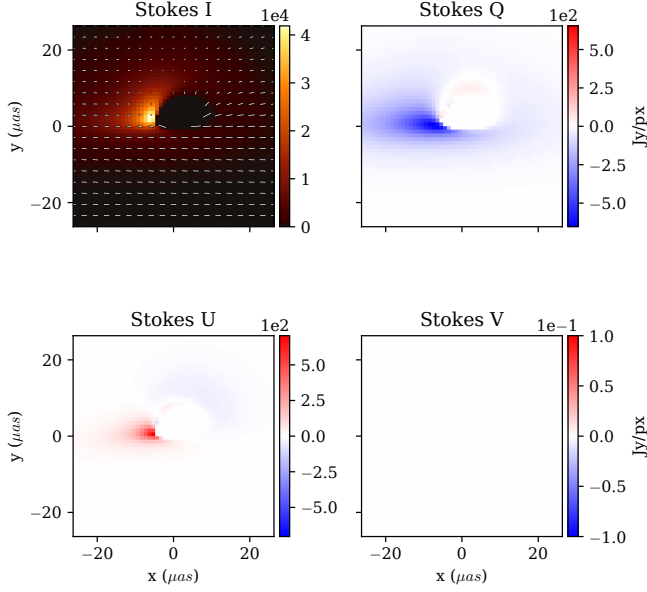


Figure 1. Example output of the thin-disk problem: the upper left panel shows total flux with overplotted polarization direction vectors scaled by the linear polarization fraction, and the other panels show fluxes of Stokes Q , U , and V at each pixel (the Stokes Q , U , and V images). In this test Stokes V remains identically zero as expected.

tests are square, with equal FOV from West to East and North to South.

For the thin-disk test, the camera parameters are:

$$\theta_{\text{cam}} = 75^\circ \quad (6a)$$

$$NX = 80 \text{ px} \quad (6b)$$

$$DX = 40 r_g \quad (6c)$$

$$\text{FOV} = 78.99 \mu\text{as} \quad (6d)$$

3.3. GRMHD Snapshot

The last test consists of imaging the relativistic thermal synchrotron emission at 230GHz from one snapshot from a GRMHD simulation. This test exercises all aspects of the code as well as code-specific choices, such as interpolation of fluid state recorded at discrete locations and calculation of the transport coefficients via fitting functions. The standard snapshot file used for this test is taken from a SANE simulation with spin $a_* = 0.9375$, performed using `iharm3D` (Prather et al. 2021) with a resolution of $288 \times 128 \times 128$ cells in r , θ , and ϕ respectively. Except for the coordinate system, this simulation exactly reflects the simulations performed with `iharm3D` as a part of the library used in EHTC V and EHTC VIII, as described in Wong et al. (2022). Not all GRRT codes can read all GRMHD output, as coordinate systems and

fluid state descriptions can differ from code to code – thus, not every polarized radiative transfer code used in the EHTC can be directly compared with this test. The `iharm3D` format is chosen as it is readable by a majority of codes used in the EHTC, and in particular those codes relevant to studies in EHTC VIII.

The snapshot is taken at $4500 r_g/c$ after simulation start, well into the run’s quiescent period. The file is available upon request for testing future codes. Since it involves creating an image from just one snapshot of the simulation, the test makes the assumption of “fast-light,” i.e., that the fluid is static as light propagates from emission to observer.

The parameters of this test are chosen to reflect values for M87*, specifically those used in creating the libraries of simulated images used in EHTC V, EHTC VI, and EHTC VIII, hereafter the “EHT image libraries.” These are:

$$M_{\text{BH}} = 6.2 \times 10^9 M_\odot \quad (7a)$$

$$D = 16.9 \text{ Mpc} \quad (7b)$$

$$\nu = 230 \text{ GHz} \quad (7c)$$

The camera is defined as in section 3.2.1, with parameters chosen to reflect the angle of the M87* jet and the FOV observed by the EHT:

$$\theta_{\text{cam}} = 163^\circ \quad (8a)$$

$$\phi_{\text{cam}} = 0^\circ \quad (8b)$$

$$\text{FOV} = 160 \mu\text{as} \quad (8c)$$

$$DX = 44.17 r_g \quad (8d)$$

$$NX = 160 \text{ px} \quad (8e)$$

In addition to the system parameters above, imaging a GRMHD simulation necessarily involves setting another scale factor which determines the density of accreting material and the strength of magnetic fields. It is expressed here as a mass unit, \mathcal{M} , which gives units to the unscaled density values from a simulation, ρ_{code} :

$$\rho_{\text{CGS}} = \frac{\mathcal{M}}{r_g^3} \rho_{\text{code}} \quad (9)$$

\mathcal{M} is not known a priori, but it is highly correlated with the total image brightness. Thus, it is scaled so as to match the total image flux density to the observed compact flux density, usually by employing an iterative solver.

In the EHT image libraries, \mathcal{M} was fit such that images taken over the course of a full simulation would produce an average of 0.5 Jy of compact flux density (see Wong et al. 2022 for details). For this test, the sample image is fit alone using `ipole-IL` such that it

produces 0.50 Jy when imaged with totally unpolarized transport, or about 0.47 Jy of Stokes I flux density when imaged using polarized transport. The value of \mathcal{M} , and the corresponding accretion rate \dot{M} , used for the test are listed below:

$$\mathcal{M} = 1.672 \cdot 10^{26} \text{ g} \quad (10a)$$

$$\dot{M} = 8.644 \cdot 10^{-5} M_{\odot}/\text{yr} = 6.285 \cdot 10^{-7} \dot{M}_{\text{Edd}} \quad (10b)$$

where \dot{M}_{Edd} is defined as earlier in this work.

Accretion flows around M87* are strongly suspected to be two-temperature, with little thermal coupling between the ions and electrons (Mahadevan & Quataert 1997; Ryan et al. 2017; Sądowski et al. 2017). Since GRMHD simulations evolve only a single fluid with a single temperature, when simulating images the internal energy must be split between the ions and electrons based on a model. While this process is not well constrained, it is generally documented which electron distribution is being assumed, and the electron energy distribution model is standardized between codes when similar performance is expected.

Thus, for simplicity, in this test we set the electron temperature to a fixed ratio of 1/3 of the ion temperature, derived from the single-fluid GRMHD parameters by holding the total internal energy constant (see EHTC V):

$$T_e = \frac{2m_p u}{15k\rho} \quad (11)$$

where u and ρ are the local fluid internal energy and rest-mass density per unit volume, respectively, and m_p and k are the proton mass and Boltzmann constant. Note that this is equivalent to the so-called “ R_{high} ” model of EHTC V with $R_{\text{low}} = R_{\text{high}} = 3$. In splitting the total internal energy rather than setting the fluid and ion temperatures equal, it differs slightly from the original statement of the R_{high} model in Mościbrodzka et al. (2016).

The emission, absorption, and rotation coefficients are calculated based on the electron temperature (or more broadly, the electron energy distribution) using fitting functions approximating the full synchrotron emission calculations, which are expensive to compute. Codes in this comparison used a few different sets of fitting functions; further discussion is found in Section 5.3 and Appendix B.

Finally, as in EHTC V and commonly in the literature, emission is tracked only from regions of the simulation with $\sigma \equiv B^2/\rho < 1$. Regions with higher sigma (largely the polar “jet” regions) can over-produce emission if included, due to hot material in the jet inserted

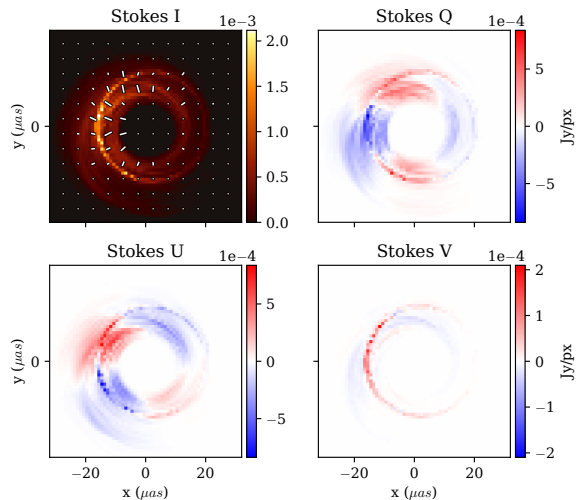


Figure 2. Example output from `ipole-IL` running the GRMHD snapshot test. The image was produced using the parameters listed in Section 3.3, with the accretion rate parameter \mathcal{M} fit so as to produce about 0.5 Jy of total flux density at 230 GHz to match EHT observations.

by numerical floors to preserve stability of GRMHD algorithms.

Example output for the GRMHD snapshot test from `ipole-IL` is provided in Figure 2.

4. RESULTS

4.1. Analytic Comparison Results

Results for the analytic integration tests from `RAPTOR`, `Odyssey`, `ipole`, and `ipole-IL` are shown in Figure 3. Raw output is plotted in the left panes, and differences from the analytic result are plotted on the right. This test verifies that the default accuracy parameters of each code allow them to match an analytic solution to within acceptable errors. Note that this is not a good measure of relative code accuracy or convergence—for convergence tests, see the accompanying code papers cited in Section 2.

Note that the results from two integrators are shown for `RAPTOR` as the “RK4” and “IE” variants. In normal integration, `RAPTOR` uses the “RK4” integrator, reserving the “IE” integrator for the few zones where Faraday rotation is too strong to take steps of an appropriate size with an explicit scheme (Bronzwaer et al. 2020).

Also, the `ipole` scheme (also used in `ipole-IL`) is semi-analytic: it uses the analytic solution for constant coefficients whenever it evolves the non-relativistic polarized radiative transfer equations. Thus, `ipole` and `ipole-IL` will perform this test *less* accurately when

taking more steps: a single step of any size would be exactly accurate, but multiple steps accrue round-off error.

4.2. Metrics

In the following two imaging tests, no exact result is available by which to evaluate code accuracy directly; rather, we evaluate consistency between all codes, both in overall image structure and in several metrics used to compare models with EHT results. In particular, we will use the definitions from [EHTC VIII](#), computed over simulated images and used to compare models to the observed EHT result. These summary statistics include the total flux density F , image-integrated or “zero-baseline” linear and circular polarization fractions $|m|_{\text{net}}$ and v_{net} , and the average linear polarization fraction over the resolved image $\langle |m| \rangle$. For an image represented as a vector of emitted flux per pixel in each Stokes parameter I_j, Q_j, U_j, V_j over each pixel j , these values are defined as:

$$F = \sum_j I_j \quad (12)$$

$$|m|_{\text{net}} = \frac{\sqrt{(\sum_j Q_j)^2 + (\sum_j U_j)^2}}{\sum_j I_j} \quad (13)$$

$$\langle |m| \rangle = \frac{\sum_j \sqrt{Q_j^2 + U_j^2}}{\sum_j I_j} \quad (14)$$

$$v_{\text{net}} = \frac{\sum_j V_j}{\sum_j I_j} \quad (15)$$

Additionally, [EHTC VIII](#) used a complex coefficient reflecting the degree and angle of azimuthally symmetric linear polarization, β_2 (see [Palumbo et al. 2020](#)). It is calculated by first centering the image, e.g., with [rex](#) ([EHTC IV](#)), and then taking the inner product of the complex linear polarization $P = Q + iU$ with a rotationally symmetric function:

$$\beta_2 = \frac{1}{I_{\text{ann}}} \int_{\rho_{\text{min}}}^{\rho_{\text{max}}} \int_0^{2\pi} P(\rho, \phi) e^{-i2\phi} \rho d\phi d\rho \quad (16)$$

$$I_{\text{ann}} = \int_{\rho_{\text{min}}}^{\rho_{\text{max}}} \int_0^{2\pi} I(\rho, \phi) \rho d\phi d\rho, \quad (17)$$

where ρ/ϕ are polar coordinates in the image plane, measured from/about the image center. This metric is expected to be useful only for images with a relatively low observer angle, as they will be more symmetric; thus it is computed and compared only for the GRMHD snapshot test, which uses the low observer angle $i = 17^\circ$

expected for M87* and used for libraries of simulated images of that object.

The quantities $\langle |m| \rangle$ and β_2 are sensitive to image resolution. In order to mirror EHT measurements and reflect how simulated images were used in [EHTC VIII](#), a circular Gaussian blur with a FWHM of $20\mu\text{as}$ was applied to all images before computing either resolution-dependent quantity.

In addition to the quantities used for direct comparison in [EHTC VIII](#), we measure a point-source linear polarization direction or electric vector position angle (EVPA) East of due North on the sky, and thus in our Stokes convention defined as:

$$\text{EVPA} = \frac{1}{2} \arg \left(\frac{\sum_j U_j}{\sum_j Q_j} \right). \quad (18)$$

As this metric is potentially volatile for images with low net linear polarization, and a corresponding measurement has not been made to which we might compare, we follow [EHTC VIII](#) in omitting this as a comparison metric – rather, we use it only in image summaries.

When evaluating image similarity, we use the normalized mean squared error (NMSE):

$$\text{NMSE}(A, B) = \frac{\sum_j |A_j - B_j|^2}{\sum_j |A_j|^2}, \quad (19)$$

where A_j and B_j are the intensities of a particular Stokes parameter in two images at pixel j . Regardless of exact nomenclature, all mean squared error values listed in this work and in [Gold et al. \(2020\)](#) use this normalization and are thus comparable.

Note that this definition of the NMSE is not symmetric under the ordering of A and B , and in particular as images get dimmer, $\text{NMSE}(I, 0) = 1$ whereas $\text{NMSE}(0, I) = \infty$. As it is normalized against the sum of squared pixel intensities, the NMSE becomes more volatile when evaluating dimmer images.

The NMSE was one of two metrics used to gauge similarity in [Gold et al. \(2020\)](#). We omit the other, the structural dissimilarity (DSSIM), since for the case of very similar images, values of the DSSIM are highly correlated with the NMSE (see [Appendix C](#)).

4.3. Thin Disk Test Results

Each code’s output for the thin disk test is plotted in [Figure 4](#). The images are visually indistinguishable except in a few particular pixels, and this similarity is borne out in the comparison metrics. Stokes V is omitted from plots and comparisons for this test, as all codes produce exactly zero Stokes V across the entire image.

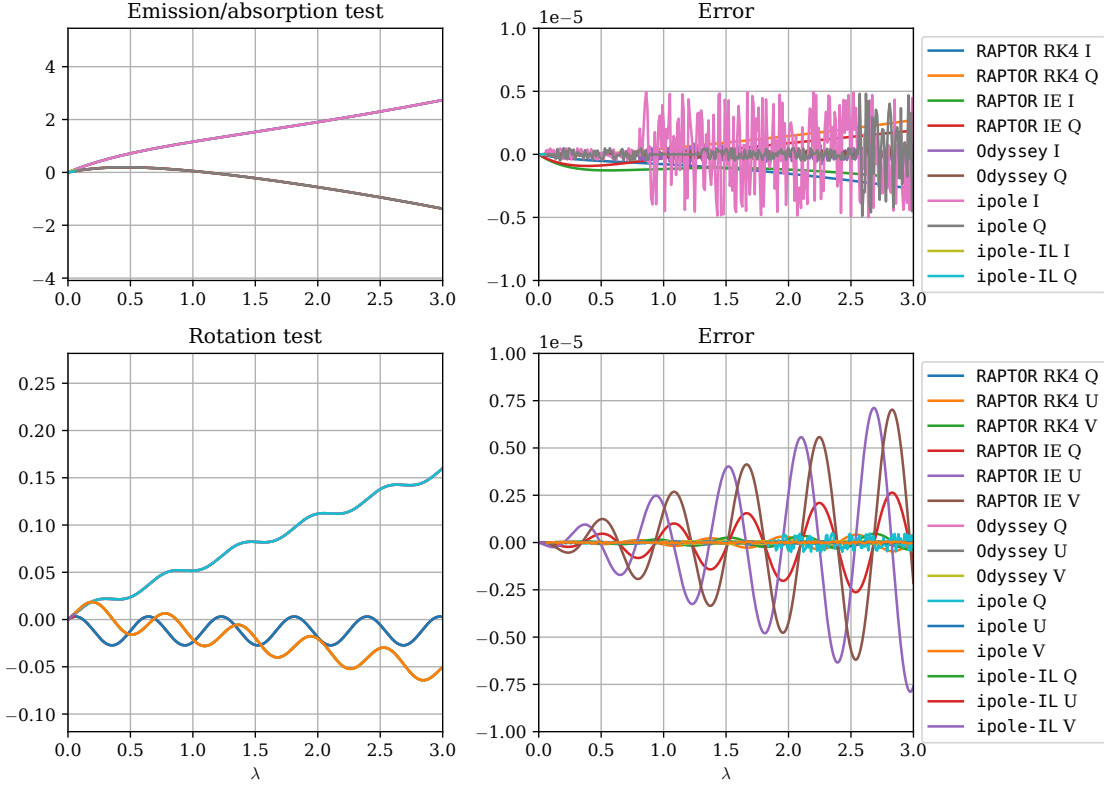


Figure 3. Comparison of integrator results for the analytic tests, plotting the relevant Stokes parameters against the dimensionless affine parameter λ , equivalent to length in this non-relativistic test. Output from all codes overlaps to within line widths in the left panes.

Recall that this test involves accurate evaluation of the geodesic equation and accurate parallel transport of the linear polarization vector from emission to camera. As the codes' similarity in tracing geodesics was evaluated extensively in Gold et al. (2020), we focus here on demonstrating the latter through comparison of the resulting Stokes Q , U images and the relevant image-integrated metrics. Table 2 lists total fluxes and net polarization parameters for each image in the test. Figure 5 presents comparisons of each metric between each pair of images.

Code	Flux [Jy]	$ m _{\text{net}}$ [%]	$\langle m \rangle$ [%]	EVPA [°]
ipole	6.841e+06	2.3341	2.378	88.123
ipole-IL	6.8699e+06	2.3224	2.3707	87.974
grtrans	6.8227e+06	2.3246	2.3709	88.01
RAPTOR	6.8689e+06	2.3265	2.3726	88.025
Odyssey	6.7338e+06	2.3527	2.3971	88.146
BHOSS	6.6949e+06	2.3439	2.3845	88.131

Table 2. Image-integrated values for the thin disk test. v_{net} is omitted as it is uniformly zero, and β_2 magnitude and angle are omitted as the image is not symmetric and thus the magnitude is very small.

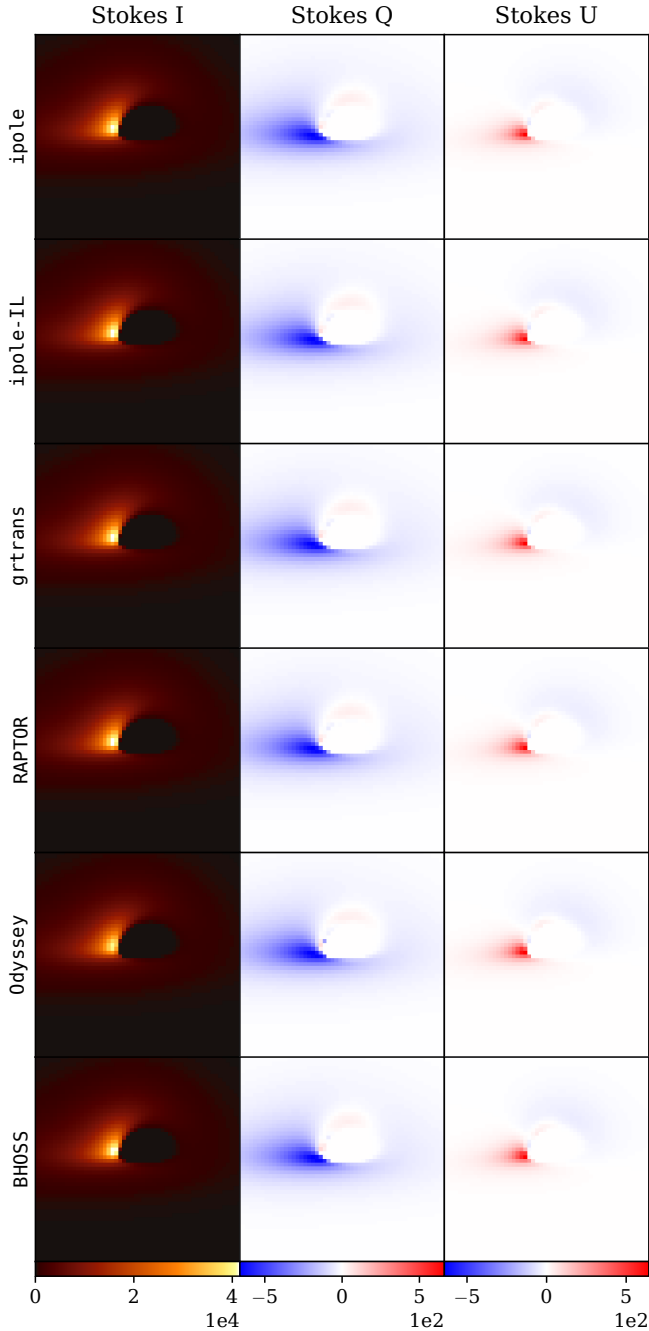


Figure 4. Full set of images produced for the thin disk problem, in which codes produced an image from an analytic prescription for an opaque thin disk. The Stokes parameters I , Q , U are plotted separately, with Stokes V omitted as it is uniformly zero.

4.4. GRMHD Snapshot Test Results

Results for the GRMHD snapshot test for `ipole`, `ipole-IL`, `grtrans`, `Odyssey`, and `RAPTOR` are listed in Table 3 and presented in Figure 7. Results are formatted similarly to the results of the thin disk test, with the addition of a Stokes V component and circular polarization fraction in images and tables and the addition of the rotationally symmetric linear polarization coefficient β_2 in tables of integrated values.

Except for the total flux density, the color bars in Figure 7 reflect the 1σ values used to make cuts when evaluating models in EHTC VIII.

5. DISCUSSION

5.1. Comparison to Observational Constraints

The values for each comparison metric used as cuts in EHTC VIII are listed in Table 4. The table values are based on 1σ ranges for measurements of the same quantities in EHT data, described in EHTC VII. These ranges provide a comparison to evaluate code interchangeability—if the differences between codes are substantially less than the range of measurement uncertainties, the analysis is agnostic to the choice of code employed. The 1σ ranges listed are also used as the color bar ranges in the colored table listings in Figure 7.

This comparison provides evidence that model evaluations as in EHTC VIII remain similar regardless of which of the included codes is employed. As recorded in Table 4, maximum code variation is universally less than 30% of the detector 1σ range: in $|m|_{\text{net}}$ (0.21% vs 1.5%), v_{net} (0.08% vs 0.4%), $\langle|m|\rangle$ (0.70% vs 2.5%), $|\beta_2|$ (0.0026 vs 0.015), and $\angle\beta_2$ (3.4° vs 17°). In any analysis based on cuts, code differences can shift a few particular images into or out of the final consideration. However, at these uncertainties no image from outside the 1σ detector uncertainty would be consistent with the central observed value.

Broadening the comparison to different images and models shows promising similarities. Appendix D presents distributions of the image differences between `ipole-IL` and `grtrans` when run over thousands of snapshots of a very different model from the example: they show a wide variance but a smaller difference on average than in the example image, suggesting that image differences, at least between these codes, are mostly stochastic, further suppressing any potential effect on a cuts-based analysis as in EHTC VIII.

5.2. Potential Measurement of System Parameters

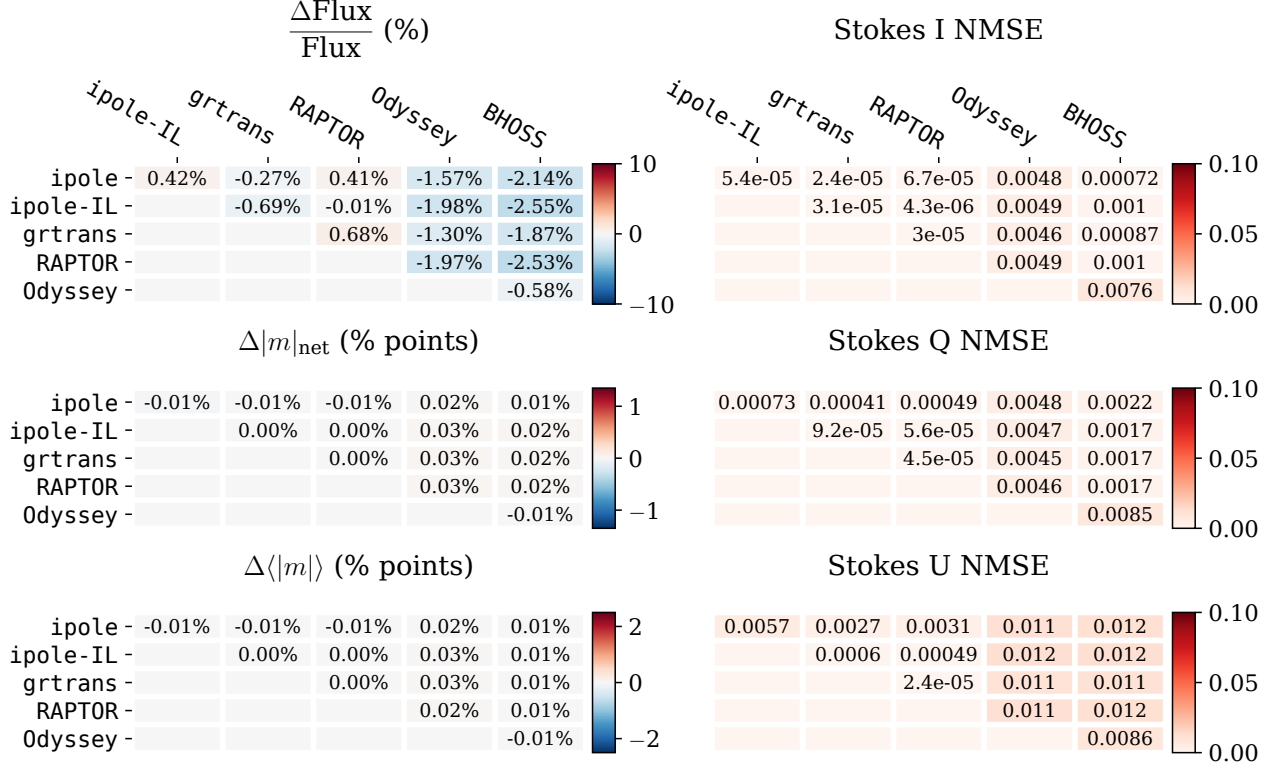


Figure 5. (left column) Tables comparing the absolute differences between the images produced by each pair of codes running the thin disk test. The values themselves are provided in Table 2. Since the differences are symmetric, the table takes only the upper triangular portion of the comparison. (right column) Tables comparing the normalized mean squared error (NMSE) between each pair of images, as defined in Section 4.2. To aid in comprehension, table cells are colored by value. Circular polarization is omitted, see test description in Section 3.2.

Code	Flux [Jy]	$ m _{\text{net}}$ [%]	v_{net} [%]	$\langle m \rangle$ [%]	EVPA [°]	$ \beta_2 $	$\angle \beta_2$ [°]
ipole-IL	0.47976	1.5232	0.64637	31.264	-78.241	0.28165	-20.307
ipole	0.47335	1.5904	0.62402	31.27	-77.243	0.28171	-20.622
RAPTOR	0.49396	1.6057	0.67381	31.893	-77.797	0.28346	-21.31
grtrans	0.45346	1.5135	0.69909	31.197	-77.647	0.28063	-17.903
Odyssey	0.46671	1.3928	0.70068	31.54	-71.432	0.28325	-20.713

Table 3. Image-integrated values for the GRMHD snapshot test. Definitions for all values are given in Section 4.2. Note that the EVPA is not used as a comparison metric in Figure 7.

To translate the NMSE into a measure of code accuracy in testing model parameters, we define an “error budget” for each Stokes parameter, consisting of the largest NMSE between code results: 0.02 in I , 0.04 in Q and U , and 0.13 in V . Assuming perfect detector accuracy and modeling, this error characterizes which images are too similar to be effectively distinguished above code-to-code variations.

We then translate this error budget into constraints on the input parameters M_{BH} , \mathcal{M} , R_{high} , and the viewing angle by varying these parameters around the nominal values and calculating the resulting MSE vs. the nominal image, using ipole-IL. As illustrated in Figure 8, the required parameter changes are very modest; that is, the possible constraints on system parameters are very precise. In imaging the example model, codes agree well enough to constrain the mass of M87* to within 0.4%

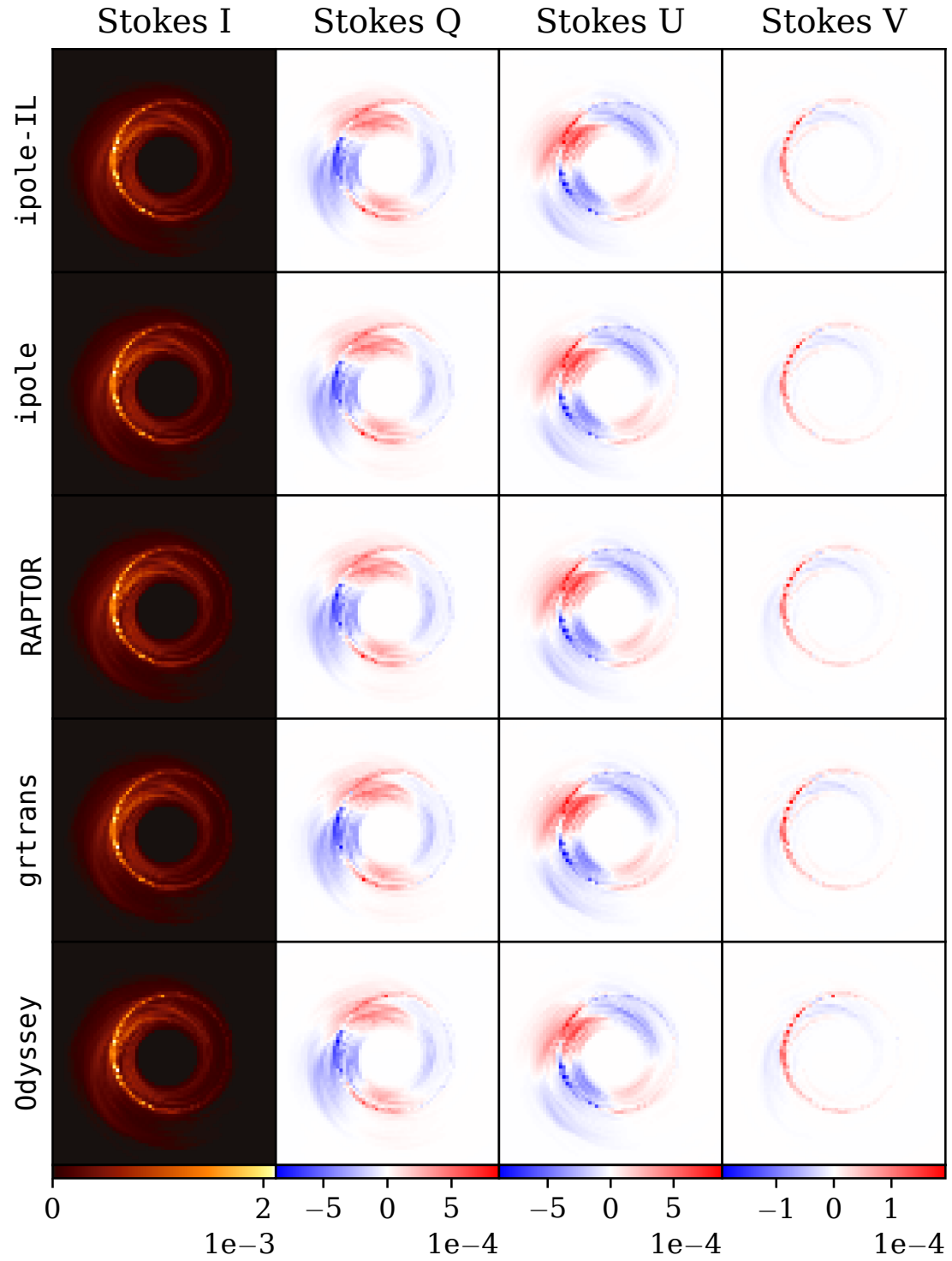


Figure 6. Comparison of images produced of the GRMHD test problem, in which codes produced an image given a simulated fluid snapshot, mirroring the analysis pipeline used in e.g. [EHTC V](#); [EHTC VIII](#). The Stokes parameters I , Q , U , V are plotted separately, with separate color bars.

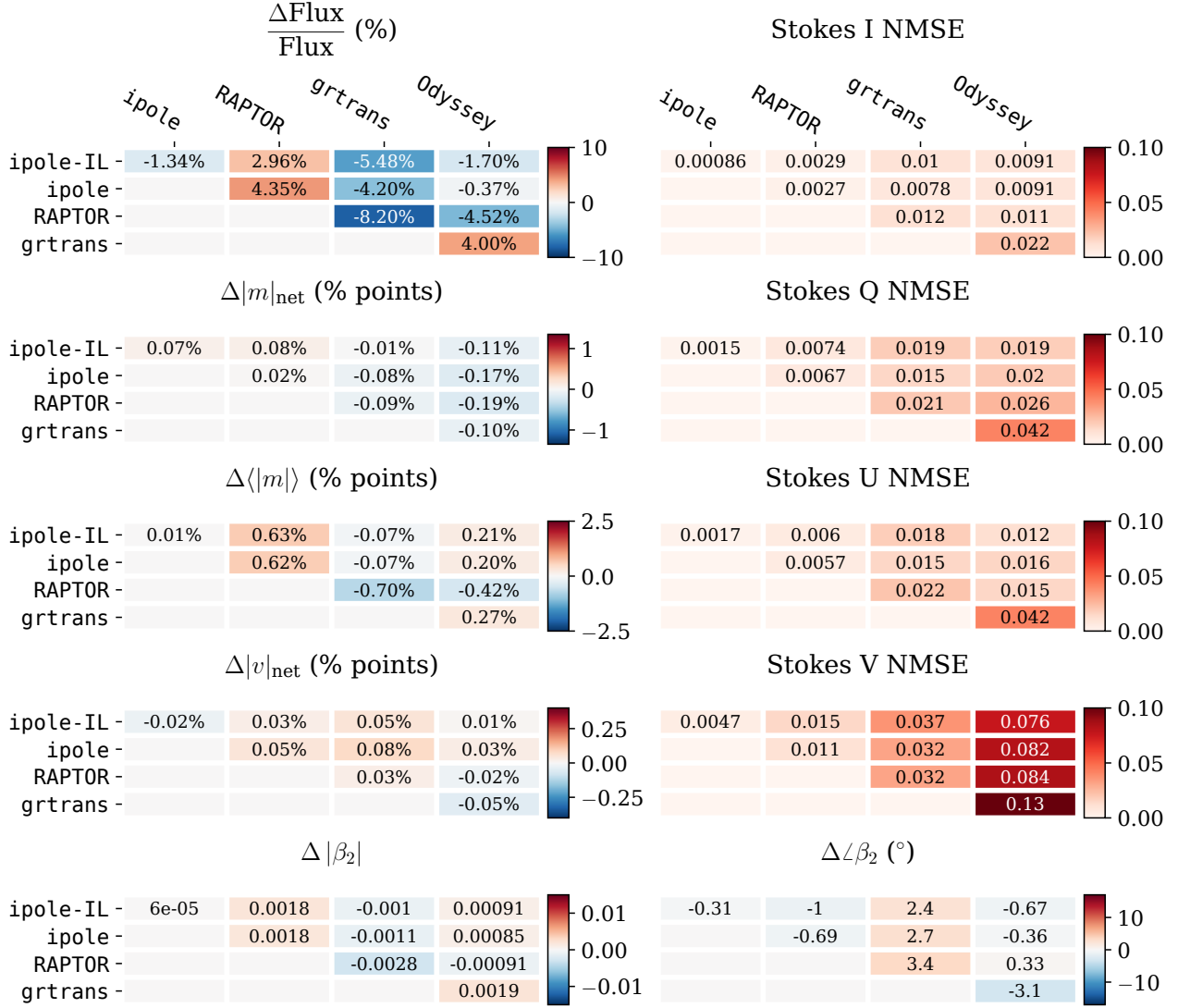


Figure 7. Tables comparing each pair of images in the GRMHD snapshot test. (left column, bottom row) Tables comparing all six image metrics used in [EHTC VIII](#). Note that except for total flux density, all comparisons are absolute: that is, images with v_{net} of 0.4% and 0.8% would be listed with a difference of 0.4% points. (right column) Tables listing the NMSE between each pair of images. See Section 4.2 for the definitions of all comparison metrics and Figure 5 for a description of table layout.

Parameter	1σ	Code Uncertainty	Uncertainty/ σ
$ m _{\text{net}}$	1.35 %	0.21 %	0.16
v_{net}	0.4 %	0.08 %	0.20
$\langle m \rangle$	2.5 %	0.70 %	0.28
$ \beta_2 $	0.015	0.0026	0.17
$\angle\beta_2$	17°	3.4°	0.20

Table 4. The “ 1σ ” column lists the 1σ detector uncertainty of each parameter, as estimated in [EHTC VII](#) and used as an allowable range when comparing models in [EHTC VIII](#). Note that the measurement of $\langle|m|\rangle$ was an upper bound; this upper bound was doubled to select the cut value. The “Code Uncertainty” column lists the greatest observed difference between codes when computing each parameter, and the final column lists this value as a proportion of the 1σ value.

($2.5 \times 10^7 M_\odot$), \mathcal{M} to 9% (1.5×10^{25}), the observer angle to 0.8° , and the R_{high} parameter to within 0.18. These values are dependent on the base image—in particular, constraints on R_{high} will also depend on R_{low} , which was set differently in this case than for images in [EHTC VIII](#).

5.3. Caveats and limitations

There are a few caveats and limitations of the ray-tracing calculations presented in this work worth mentioning and improving in the future. Most glaringly, all ray-tracing codes use phenomenological post-processing models of the electron energy distribution. In particular, this comparison adopts a fixed ratio of ion to electron temperature, which is not well-motivated by EHT results. More accurate temperature prescriptions including cold electrons in the accretion disk dramatically increase Faraday rotation when viewed from the equator, scrambling the emission angle over regions of the image. Scrambled emission does not affect the total intensity image, nor the measurable quantities in this comparison (except $\angle\beta_2$, which only makes sense to measure for face-on images with low Faraday scrambling). Detailed study of code behavior in imaging Faraday-scrambled regions is left for future work.

All ray-tracing codes use synchrotron emissivities/absorptivities/rotativities in analytic forms which are fit formulas to synchrotron emissions integrated over (most often thermal) electron distribution function. The fit functions may differ from code to code and from the true emissivity and therefore introduce a small error to the integration. We discuss this issue in more detail in [Appendix B](#). Other caveats concern the common assumption that the electrons are distributed isotropically, which may not be a good approximation for collisionless plasma surrounding Sgr A* and M87*.

Calculations presented in this work assume the infinite speed of light (so called fast-light approximation) while in reality the light propagation timescale is comparable to the plasma dynamical timescale near the event horizon of the black hole. Any future comparison of ray-tracing codes should include finite light propagation time effects. In such future comparison another source of error could be the time-interpolations between GRMHD model time slices.

Finally, the linear polarization and the EVPA are sensitive to the external Faraday screen made of mildly or non-relativistic electrons (which in practice could be located thousands of M away from the black hole). Any inconsistencies in choosing the outer boundary of the ray-tracing integration may introduce discrepancies in the linear polarization maps. The latter is not specific caveat of the ray-tracing itself but it is a limitation when comparing models to observations.

6. CONCLUSIONS

In each of the tests conducted for this comparison, the several general-relativistic radiative transfer codes used within the EHT Collaboration have produced sufficiently similar results that they are functionally interchangeable for the collaboration’s uses. This is true both when measured in terms of image similarity (mean squared error) and when measured directly in terms of the image metrics used to compare simulated polarized images to the EHT result in [EHTC VIII](#).

Using their default accuracy parameters, codes match the analytic result for the case of constant transport coefficients to better than 1 part in 10^{-5} . They agree to within 1.5% mean squared error when imaging an analytically-defined problem requiring parallel transport of the polarization vector.

In the more complex task of interpolating, translating, and imaging GRMHD output, codes agree to within a normalized mean squared error of 0.13 at worst, when measuring specifically the circular polarization map (NMSE of 0.045 in linear polarization, 0.02 in total intensity). Based on image similarity, the choice of imaging code will matter in model comparisons only when trying to determine the BH mass to within 0.4%, accretion rate within 9%, or observer angle to within 0.8° . These values significantly outclass both the detection and modeling uncertainties available in the near future.

When measured with the image metrics used for model comparison in [EHTC VIII](#), all comparison images agree to much better precision than the detector uncertainty. Further, much of the difference which does appear is shown to be stochastic in nature. Thus the

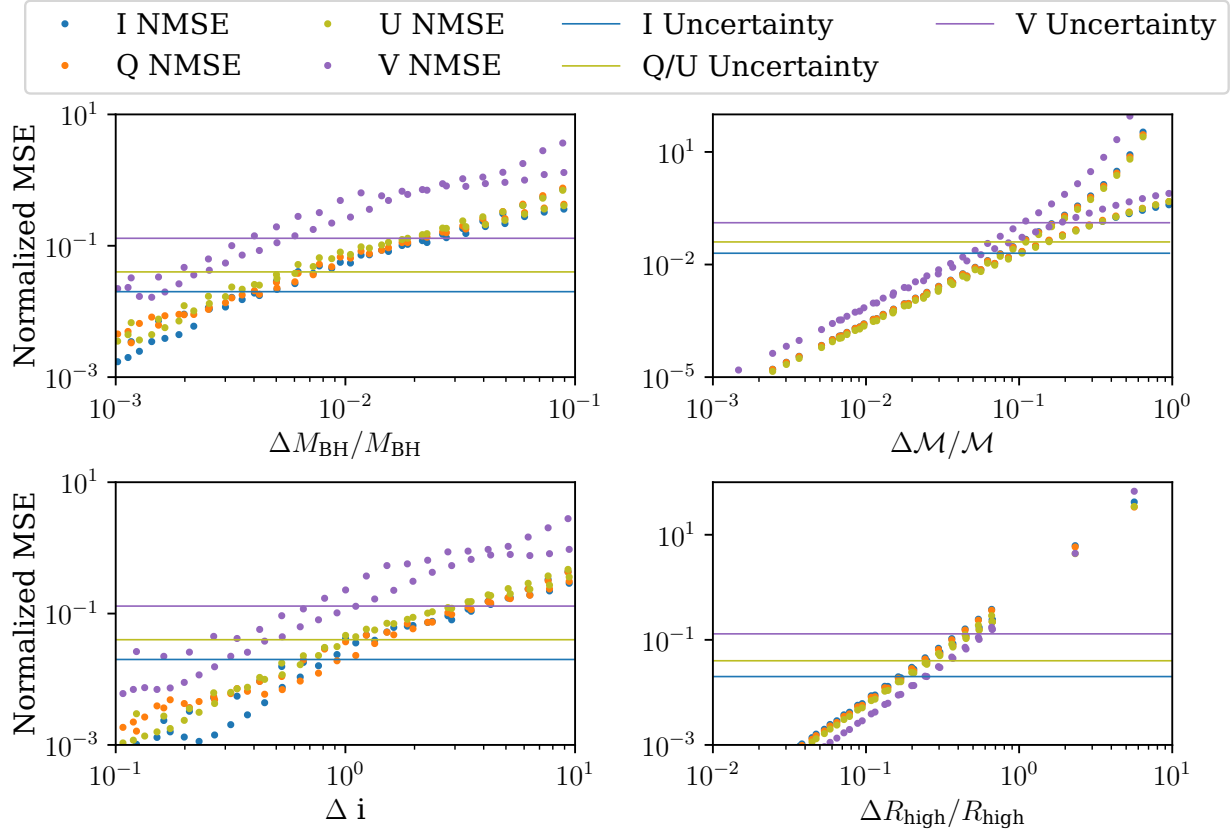


Figure 8. Plots of image mean squared error produced when varying several parameters (BH mass, angle, R_{high} , and accretion rate) around values used for the GRMHD snapshot test. For each difference, plotted along the x axis, images were run with the parameter increased and decreased by that amount, resulting in two NMSE values, which are then overplotted. The largest NMSE between codes is plotted to provide a visual ceiling on “indistinguishable” images. Based on code agreement, current transport schemes can constrain all input parameters much more accurately than current models and detectors.

choice of code is verified directly to have little effect on the analysis performed in that paper.

7. ACKNOWLEDGEMENTS

The Event Horizon Telescope Collaboration thanks the following organizations and programs: the Academia Sinica; the Academy of Finland (projects 274477, 284495, 312496, 315721); the Agencia Nacional de Investigación y Desarrollo (ANID), Chile via NCN19_058 (TITANs) and Fondecyt 1221421, the Alexander von Humboldt Stiftung; an Alfred P. Sloan Research Fellowship; Allegro, the European ALMA Regional Centre node in the Netherlands, the NL astronomy research network NOVA and the astronomy institutes of the University of Amsterdam, Leiden University and Radboud University; the ALMA North America Development Fund; the Black Hole Initiative, which is funded by grants from the John Templeton Foundation and the Gordon and Betty Moore Foundation (although the opinions expressed in this work are those of the author(s) and do not necessarily reflect the views of these Foundations); the

Brinson Foundation; Chandra DD7-18089X and TM6-17006X; the China Scholarship Council; the China Postdoctoral Science Foundation fellowships (2020M671266, 2022M712084); Consejo Nacional de Ciencia y Tecnología (CONACYT, Mexico, projects U0004-246083, U0004-259839, F0003-272050, M0037-279006, F0003-281692, 104497, 275201, 263356); the Consejería de Economía, Conocimiento, Empresas y Universidad of the Junta de Andalucía (grant P18-FR-1769), the Consejo Superior de Investigaciones Científicas (grant 2019AEP112); the Delaney Family via the Delaney Family John A. Wheeler Chair at Perimeter Institute; Dirección General de Asuntos del Personal Académico-Universidad Nacional Autónoma de México (DGAPA-UNAM, projects IN112417 and IN112820); the Dutch Organization for Scientific Research (NWO) for VICI award (grant 639.043.513), grant OCENW.KLEIN.113 and the Dutch Black Hole Consortium (with project number NWA 1292.19.202) of the research programme the National Science Agenda; the Dutch National Supercomputers, Cartesius and Snellius (NWO Grant

2021.013); the EACOA Fellowship awarded by the East Asia Core Observatories Association, which consists of the Academia Sinica Institute of Astronomy and Astrophysics, the National Astronomical Observatory of Japan, Center for Astronomical Mega-Science, Chinese Academy of Sciences, and the Korea Astronomy and Space Science Institute; the European Research Council (ERC) Synergy Grant “BlackHoleCam: Imaging the Event Horizon of Black Holes” (grant 610058); the European Union Horizon 2020 research and innovation programme under grant agreements RadioNet (No 730562) and M2FINDERS (No 101018682); the Horizon ERC Grants 2021 programme under grant agreement No. 101040021; the Generalitat Valenciana post-doctoral grant APOSTD/2018/177 and GenT Program (project CIDEAGENT/2018/021); MICINN Research Project PID2019-108995GB-C22; the European Research Council for advanced grant ‘JETSET: Launching, propagation and emission of relativistic jets from binary mergers and across mass scales’ (Grant No. 884631); the Institute for Advanced Study; the Istituto Nazionale di Fisica Nucleare (INFN) sezione di Napoli, iniziative specifiche TEONGRAV; the International Max Planck Research School for Astronomy and Astrophysics at the Universities of Bonn and Cologne; DFG research grant “Jet physics on horizon scales and beyond” (Grant No. FR 4069/2-1); Joint Columbia/Flatiron Postdoctoral Fellowship, research at the Flatiron Institute is supported by the Simons Foundation; the Japan Ministry of Education, Culture, Sports, Science and Technology (MEXT; grant JPMXP1020200109); the Japan Society for the Promotion of Science (JSPS) Grant-in-Aid for JSPS Research Fellowship (JP17J08829); the Joint Institute for Computational Fundamental Science, Japan; the Key Research Program of Frontier Sciences, Chinese Academy of Sciences (CAS, grants QYZDJ-SSW-SLH057, QYZDJSSW-SYS008, ZDBS-LY-SLH011); the Leverhulme Trust Early Career Research Fellowship; the Max-Planck-Gesellschaft (MPG); the Max Planck Partner Group of the MPG and the CAS; the MEXT/JSPS KAKENHI (grants 18KK0090, JP21H01137, JP18H03721, JP18K13594, 18K03709, JP19K14761, 18H01245, 25120007); the Malaysian Fundamental Research Grant Scheme (FRGS) FRGS/1/2019/STG02/UM/02/6; the MIT International Science and Technology Initiatives (MISTI) Funds; the Ministry of Science and Technology (MOST) of Taiwan (103-2119-M-001-010-MY2, 105-2112-M-001-025-MY3, 105-2119-M-001-042, 106-2112-M-001-011, 106-2119-M-001-013, 106-2119-M-001-027, 106-2923-M-001-005, 107-2119-M-001-017, 107-2119-M-001-020, 107-2119-M-001-041, 107-2119-M-110-

005, 107-2923-M-001-009, 108-2112-M-001-048, 108-2112-M-001-051, 108-2923-M-001-002, 109-2112-M-001-025, 109-2124-M-001-005, 109-2923-M-001-001, 110-2112-M-003-007-MY2, 110-2112-M-001-033, 110-2124-M-001-007, and 110-2923-M-001-001); the Ministry of Education (MoE) of Taiwan Yushan Young Scholar Program; the Physics Division, National Center for Theoretical Sciences of Taiwan; the National Aeronautics and Space Administration (NASA, Fermi Guest Investigator grant 80NSSC20K1567, NASA Astrophysics Theory Program grant 80NSSC20K0527, NASA NuSTAR award 80NSSC20K0645); NASA Hubble Fellowship grants HST-HF2-51431.001-A, HST-HF2-51482.001-A awarded by the Space Telescope Science Institute, which is operated by the Association of Universities for Research in Astronomy, Inc., for NASA, under contract NAS5-26555; the National Institute of Natural Sciences (NINS) of Japan; the National Key Research and Development Program of China (grant 2016YFA0400704, 2017YFA0402703, 2016YFA0400702); the National Science Foundation (NSF, grants AST-0096454, AST-0352953, AST-0521233, AST-0705062, AST-0905844, AST-0922984, AST-1126433, AST-1140030, DGE-1144085, AST-1207704, AST-1207730, AST-1207752, MRI-1228509, OPP-1248097, AST-1310896, AST-1440254, AST-1555365, AST-1614868, AST-1615796, AST-1715061, AST-1716327, AST-1716536, OISE-1743747, AST-1816420, AST-1935980, AST-2034306); NSF Astronomy and Astrophysics Postdoctoral Fellowship (AST-1903847); the Natural Science Foundation of China (grants 11650110427, 10625314, 11721303, 11725312, 11873028, 11933007, 11991052, 11991053, 12192220, 12192223); the Natural Sciences and Engineering Research Council of Canada (NSERC, including a Discovery Grant and the NSERC Alexander Graham Bell Canada Graduate Scholarships-Doctoral Program); the National Youth Thousand Talents Program of China; the National Research Foundation of Korea (the Global PhD Fellowship Grant: grants NRF-2015H1A2A1033752, the Korea Research Fellowship Program: NRF-2015H1D3A1066561, Brain Pool Program: 2019H1D3A1A01102564, Basic Research Support Grant 2019R1F1A1059721, 2021R1A6A3A01086420, 2022R1C1C1005255); Netherlands Research School for Astronomy (NOVA) Virtual Institute of Accretion (VIA) postdoctoral fellowships; Onsala Space Observatory (OSO) national infrastructure, for the provisioning of its facilities/observational support (OSO receives funding through the Swedish Research Council under grant 2017-00648); the Perimeter Institute for Theoretical Physics (research at Perimeter Institute is supported by the Government of Canada through the Depart-

ment of Innovation, Science and Economic Development and by the Province of Ontario through the Ministry of Research, Innovation and Science); the Princeton Gravity Initiative; the Spanish Ministerio de Ciencia e Innovación (grants PGC2018-098915-B-C21, AYA2016-80889-P, PID2019-108995GB-C21, PID2020-117404GB-C21); the University of Pretoria for financial aid in the provision of the new Cluster Server nodes and SuperMicro (USA) for a SEEDING GRANT approved towards these nodes in 2020; the Shanghai Pilot Program for Basic Research, Chinese Academy of Science, Shanghai Branch (JCYJ-SHFY-2021-013); the State Agency for Research of the Spanish MCIU through the “Center of Excellence Severo Ochoa” award for the Instituto de Astrofísica de Andalucía (SEV-2017- 0709); the Spinoza Prize SPI 78-409; the South African Research Chairs Initiative, through the South African Radio Astronomy Observatory (SARAO, grant ID 77948), which is a facility of the National Research Foundation (NRF), an agency of the Department of Science and Innovation (DSI) of South Africa; the Toray Science Foundation; the Swedish Research Council (VR); the US Department of Energy (USDOE) through the Los Alamos National Laboratory (operated by Triad National Security, LLC, for the National Nuclear Security Administration of the USDOE (Contract 89233218CNA000001); and the YCAA Prize Postdoctoral Fellowship.

We thank the staff at the participating observatories, correlation centers, and institutions for their enthusiastic support. This paper makes use of the following ALMA data: ADS/JAO.ALMA#2016.1.01154.V. ALMA is a partnership of the European Southern Observatory (ESO; Europe, representing its member states), NSF, and National Institutes of Natural Sciences of Japan, together with National Research Council (Canada), Ministry of Science and Technology (MOST; Taiwan), Academia Sinica Institute of Astronomy and Astrophysics (ASIAA; Taiwan), and Korea Astronomy and Space Science Institute (KASI; Republic of Korea), in cooperation with the Republic of Chile. The Joint ALMA Observatory is operated by ESO, Associated Universities, Inc. (AUI)/NRAO, and the National Astronomical Observatory of Japan (NAOJ). The NRAO is a facility of the NSF operated under cooperative agreement by AUI. This research used resources of the Oak Ridge Leadership Computing Facility at the Oak Ridge National Laboratory, which is supported by the Office of Science of the U.S. Department of Energy under Contract No. DE-AC05-00OR22725. We also thank the Center for Computational Astrophysics, National Astronomical Observatory of Japan. The computing cluster of Shanghai VLBI correlator supported by the Special

Fund for Astronomy from the Ministry of Finance in China is acknowledged. This work was supported by FAPESP (Fundacao de Amparo a Pesquisa do Estado de Sao Paulo) under grant 2021/01183-8.

APEX is a collaboration between the Max-Planck-Institut für Radioastronomie (Germany), ESO, and the Onsala Space Observatory (Sweden). The SMA is a joint project between the SAO and ASIAA and is funded by the Smithsonian Institution and the Academia Sinica. The JCMT is operated by the East Asian Observatory on behalf of the NAOJ, ASIAA, and KASI, as well as the Ministry of Finance of China, Chinese Academy of Sciences, and the National Key Research and Development Program (No. 2017YFA0402700) of China and Natural Science Foundation of China grant 11873028. Additional funding support for the JCMT is provided by the Science and Technologies Facility Council (UK) and participating universities in the UK and Canada. The LMT is a project operated by the Instituto Nacional de Astrófisica, Óptica, y Electrónica (Mexico) and the University of Massachusetts at Amherst (USA). The IRAM 30-m telescope on Pico Veleta, Spain is operated by IRAM and supported by CNRS (Centre National de la Recherche Scientifique, France), MPG (Max-Planck-Gesellschaft, Germany) and IGN (Instituto Geográfico Nacional, Spain). The SMT is operated by the Arizona Radio Observatory, a part of the Steward Observatory of the University of Arizona, with financial support of operations from the State of Arizona and financial support for instrumentation development from the NSF. Support for SPT participation in the EHT is provided by the National Science Foundation through award OPP-1852617 to the University of Chicago. Partial support is also provided by the Kavli Institute of Cosmological Physics at the University of Chicago. The SPT hydrogen maser was provided on loan from the GLT, courtesy of ASIAA.

This work used the Extreme Science and Engineering Discovery Environment (XSEDE), supported by NSF grant ACI-1548562, and CyVerse, supported by NSF grants DBI-0735191, DBI-1265383, and DBI-1743442. XSEDE Stampede2 resource at TACC was allocated through TG-AST170024 and TG-AST080026N. XSEDE JetStream resource at PTI and TACC was allocated through AST170028. This research is part of the Frontera computing project at the Texas Advanced Computing Center through the Frontera Large-Scale Community Partnerships allocation AST20023. Frontera is made possible by National Science Foundation award OAC-1818253. This research was done using services provided by the OSG Consortium (Pordes et al. 2007; Sfiligoi et al. 2009), which is supported by the National Science Foundation awards #2030508 and #1836650.

Additional work used ABACUS2.0, which is part of the eScience center at Southern Denmark University. Simulations were also performed on the SuperMUC cluster at the LRZ in Garching, on the LOEWE cluster in CSC in Frankfurt, on the HazelHen cluster at the HLRS in Stuttgart, and on the Pi2.0 and Siyuan Mark-I at Shanghai Jiao Tong University. The computer resources of the Finnish IT Center for Science (CSC) and the Finnish Computing Competence Infrastructure (FCCI) project are acknowledged. This research was enabled in part by support provided by Compute Ontario (<http://computeontario.ca>), Calcul Quebec (<http://www.calculquebec.ca>) and Compute Canada (<http://www.computecanada.ca>).

The EHTC has received generous donations of FPGA chips from Xilinx Inc., under the Xilinx University Program. The EHTC has benefited from technology

shared under open-source license by the Collaboration for Astronomy Signal Processing and Electronics Research (CASPER). The EHT project is grateful to T4Science and Microsemi for their assistance with Hydrogen Masers. This research has made use of NASA’s Astrophysics Data System. We gratefully acknowledge the support provided by the extended staff of the ALMA, both from the inception of the ALMA Phasing Project through the observational campaigns of 2017 and 2018. We would like to thank A. Deller and W. Brisken for EHT-specific support with the use of DiFX. We thank Martin Shepherd for the addition of extra features in the Difmap software that were used for the CLEAN imaging results presented in this paper. We acknowledge the significance that Maunakea, where the SMA and JCMT EHT stations are located, has for the indigenous Hawaiian people.

APPENDIX

A. COMPARISON OF POLARIZED SPECTRA FROM IMAGING AND MONTE CARLO RADIATIVE TRANSFER METHODS

In all imaging ray tracing codes radiative transfer equations are solved along null-geodesics that terminate at a “camera” at some large distance from the supermassive black holes and where a polarization map at a chosen observing frequency is constructed. By integrating Stokes parameters over entire images made for different frequencies one can also construct a polarized synchrotron spectral energy distribution of any model. However instead of comparing model spectra from the discussed imaging codes here we carry out an alternative comparison. Namely we compare spectra produced by `ipole` code to polarized spectra generated via Monte Carlo scheme `radpol`. In Monte Carlo code the polarized radiative transfer integration scheme is conceptually distinct from all discussed imaging codes (for detailed description see Mościbrodzka 2020). Showing a convergence of two different approaches is an independent validation of emission produced by imaging codes. Hence, we compare spectra produced by `ipole` and `radpol` codes using plasma model setup described in Section 3.3 (the test with \mathcal{M}_{10w}). In Figure 9, we show radio-millimeter spectra of Stokes I luminosity, fractional linear polarization and circular polarizations. The relative difference between luminosities is less than 10%, except for high frequency emission. Both codes show consistent amplitude of fractional linear and circular polarizations and agree on handedness of circular polarization.

B. EFFECT OF POLARIZED EMISSIVITY AND ROTATIVITY FITS

The emission, absorption, and rotation coefficients of a fluid are well-determined for a particular distribution of electron energies. However, the integrations involved are numerically expensive; since the coefficients must be calculated at every step when integrating the radiative transfer equations, fitting functions have been developed to approximate the coefficients quickly. A few sets of such fitting functions exist applicable to our regime; one outlined in Dexter (2016), the other in Pandya et al. (2016) and Marszewski et al. (2021).

The differences between these functions at various points within a representative set of input parameters are given in their respective papers, but we wish to provide some intuition concerning the differences these functions make in practice, and consequently whether fitting accuracy might be a driving factor in code differences.

All of the images in this comparison were created using the coefficient fits from Dexter (2016). Substituting the coefficient fits from Pandya et al. (2016) produces results more dissimilar than the disagreement between codes on three metrics: the net circular polarization at 0.13 points rather than 0.08 points, and average linear polarization fraction at 1.8 points rather than 0.7 points, and the $|\beta_2|$ coefficient at 0.016 rather than 0.0026. This is due to significant differences between the fits in computing the emission coefficient for circularly polarized light, j_V .

Image run with...	NMSE I	NMSE Q	NMSE U	NMSE V	$\Delta m _{\text{net}}$ [%]	$\Delta\langle m \rangle$ [%]	Δv_{net} [%]	$\Delta \beta_2 $	$\Delta\angle\beta_2$ [°]
...Pandya j_S	4.7e-05	0.0055	0.0059	0.0087	0.0246	1.78	0.127	0.0168	0.353
...Dexter ρ_V	1.4e-09	2.6e-06	2.1e-06	6.8e-06	-0.00746	0.0186	-0.0031	0.000131	0.00225
...approx. $K_n(x)$	3.9e-08	5.6e-05	2.5e-05	0.00014	-0.000404	0.0239	-0.00524	0.000123	-0.00336

Table 5. Comparison of changes to the `ipole-IL` result under different emission coefficient fitting functions. Each row lists a change made to the default emissivity values and the resulting differences between the new image and the one used in the comparison. Substituting emissivities from Pandya et al. (2016) changes the result by more than the overall level of code agreement, whereas substituting the ρ_V fit from Dexter (2016) changes almost nothing about the image. Approximating the Bessel functions K_n does not badly affect this image, but can be a substantial source of error in images with higher Faraday rotation.

Unlike most emission coefficients, Faraday rotation coefficient ρ_V does not go to zero with low temperature – therefore the low-temperature behavior of fitting functions is important. In particular, the expression from Dexter (2016) for ρ_V should not be used at low temperature $\Theta_e < 1$, since it can produce a catastrophic cancellation not matching the desired limiting behavior of one of its quotients. Due to this instability, most codes either switch to the Shcherbakov fit at low temperature (e.g., `grtrans`), or use the Shcherbakov fit exclusively (e.g., `ipole-IL`). As illustrated in Table 5 these approaches produce nearly identical results, different by a mean squared error less than 10^{-5} in the worst case.

Also, both the expressions from Shcherbakov (2008) and Dexter (2016) involve Bessel functions, which are tempting to approximate by assuming emission is exclusive to the regime $\Theta_e > 1$ in order to avoid unnecessary computation. However, this approximation produces clearly incorrect limiting behavior for ρ_V at low temperature. Thus the Faraday rotation is misapplied, producing too little rotation in the EVPA, or in some cases, rotation in the wrong direction. In the sample image this is a minor effect due to an overall small Faraday rotation, but it can severely affect SANE disks seen from larger observer angles.

C. COMPARISON BETWEEN IMAGE DIFFERENCE METRICS

In addition to the mean squared error, several other metrics could be used to gauge image dissimilarity between codes. Three additional metrics were evaluated in the context of this comparison: the normalized mean linear error (NMLE), structural dissimilarity (DSSIM), and inverse zero-normalized cross correlation (DZNCC). These are defined as follows:

$$\text{NMLE}(A, B) = \frac{\sum_j |A_j - B_j|}{\sum_j |A_j|} \quad (\text{C1})$$

$$\begin{aligned} \text{SSIM}(A, B) &= \left(\frac{2\mu_A\mu_B}{\mu_A^2 + \mu_B^2} \right) \\ &\times \left(\frac{\frac{2}{N} \sum_j (A_j - \mu_A)(B_j - \mu_B)}{\sigma_A^2 + \sigma_B^2} \right) \end{aligned} \quad (\text{C2})$$

$$\text{DSSIM}(A, B) = \frac{1}{|\text{SSIM}(A, B)|} - 1 \quad (\text{C3})$$

$$\text{ZNCC}(A, B) = \frac{1}{N} \sum_j \frac{1}{\sigma_A\sigma_B} (A_j - \mu_A)(B_j - \mu_B) \quad (\text{C4})$$

$$\text{DZNCC}(A, B) = \frac{1}{|\text{ZNCC}(A, B)|} - 1 \quad (\text{C5})$$

where μ_X is the average pixel value of an image and σ_X is the standard deviation of the pixel values.

In this comparison, most images were very similar—for this limited case, the various similarity metrics were found to correlate strongly in ordering of similarity between all images, and usually even in relative magnitude, as shown in Figure 10. The absolute values of the constraint metrics mean little without the context of Section 5.2, so any particular metric could fill the role of a similarity gauge to compare to image variation from other sources.

D. COMPARISON OF IMAGES OVER FULL GRMHD RUN

While the GRMHD snapshot file used for the test in 3.3 reflects the simulations and imaging parameters used in practice by the EHTC in studies of M87*, there is always the chance that the snapshot itself is a particularly simple case, not reflective of average code differences in practice. Furthermore, in characterizing the impact of code differences on metric-based model comparisons, it would be useful to have an idea of what portion of code differences in metrics are due to systematic errors,

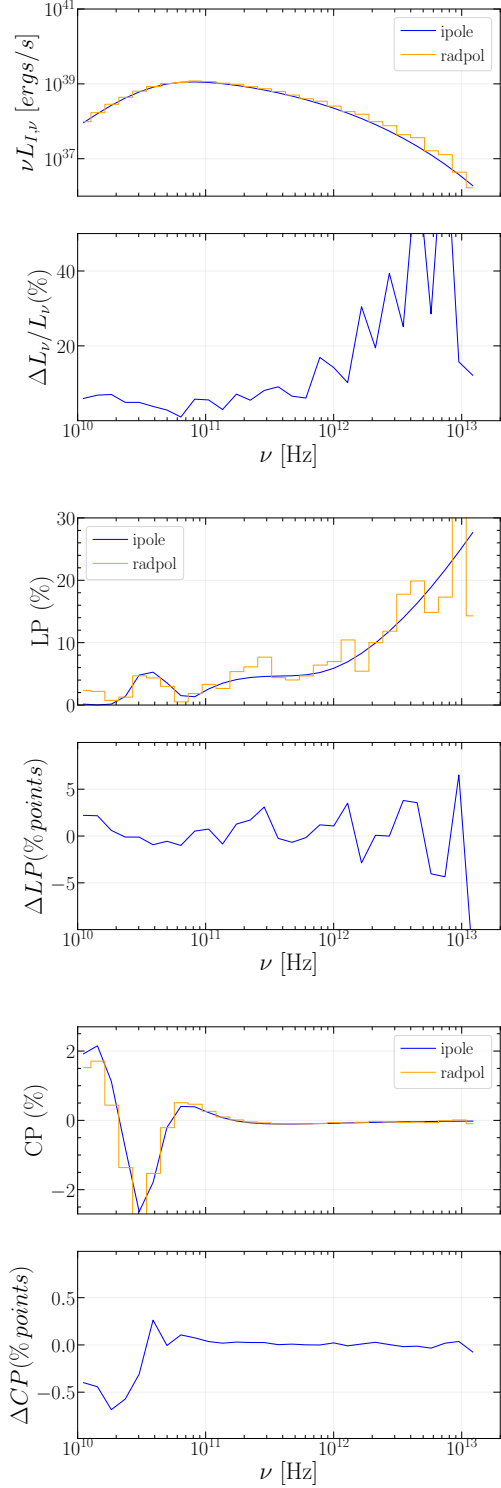


Figure 9. Comparison of luminosity, fractional linear and circular polarizations across synchrotron spectrum produced by `ipole` and `radpol` codes using SANE simulation with the same parameters. Both radiative transfer schemes show consistent amplitude of fractional linear and circular polarizations and agree on handedness of circular polarization.

Variable	μ	σ	μ/σ
$\frac{\Delta \text{Flux}}{\text{Flux}}$ (%)	-0.197	0.841	0.234
$\Delta m _{\text{net}}$ (%)	-0.0627	0.27	0.232
$\Delta \langle m \rangle$ (%)	-0.0182	0.206	0.0884
$\Delta v _{\text{net}}$ (%)	0.00168	0.0116	0.145
$\Delta \beta_2 $	-0.00178	0.00361	0.493
$\Delta \angle \beta_2$ (°)	-0.0757	1.31	0.0576

Table 6. Mean values and standard deviations of the distributions in Figure 11. The last column lists the proportion μ/σ , which can be taken as an estimate of the relevance of systematic vs stochastic errors in describing differences between these codes.

vs. stochastic products of limited accuracy parameters or sampling differences.

To measure the variation in results of this test over a typical variety of GRMHD states, two codes with substantially different algorithms, `ipole-IL` and `grtrans`, were compared across 2,000 snapshots of a GRMHD simulation used in generating the EHT image libraries. This particular simulation represented a magnetically arrested disk (MAD) state about a BH of spin $a_* = 0.9375$, and the 2,000 snapshots shown represent the entire quiescent portion of the simulation from $5,000 r_g/c$ to $15,000 r_g/c$. Details of the initial conditions, resolution, etc. are available in [Wong et al. \(2022\)](#).

Figure 11 compares the total unpolarized flux computed by `ipole-IL` and `grtrans` over the entire window. The lower plots provide histograms of the differences in all image-integrated values over the window, along with Gaussian functions following their means and standard deviations. Table 6 lists the mean (i.e., average difference) and standard deviation (i.e., span of differences) between codes in each metric. The parameters $\langle |m| \rangle$ and $\angle \beta_2$ appear to be almost entirely stochastic. Flux, $|m|_{\text{net}}$, and v_{net} are approximately a quarter systematic, and $|\beta_2|$ is half systematic (though the error itself is minuscule).

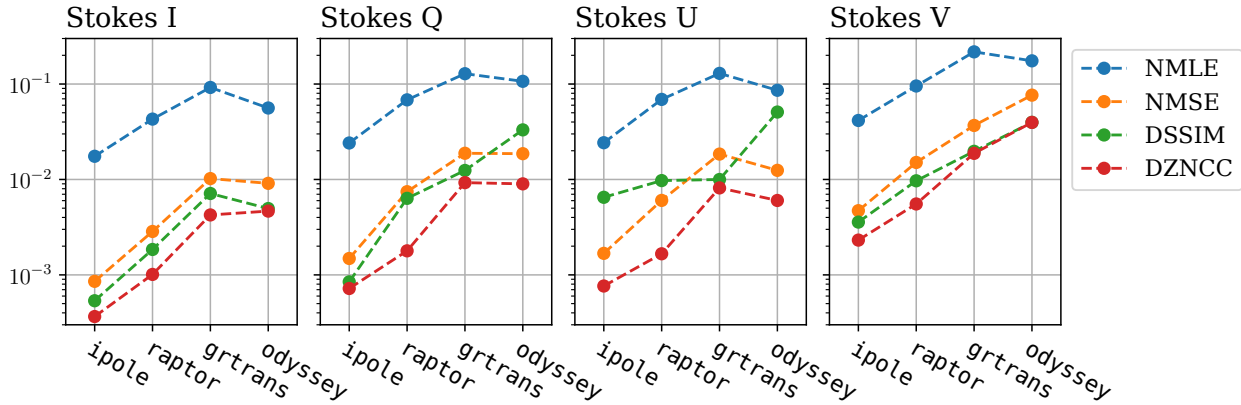


Figure 10. Each Stokes parameter of the *ipole*-IL image result for the high- \mathcal{M} GRMHD snapshot test, evaluated against each other code using 4 different metrics (all normalized): the mean linear error (MLE), mean squared error (MSE), structural dissimilarity (DSSIM), and inverse zero-normalized cross-correlation (DZNCC).

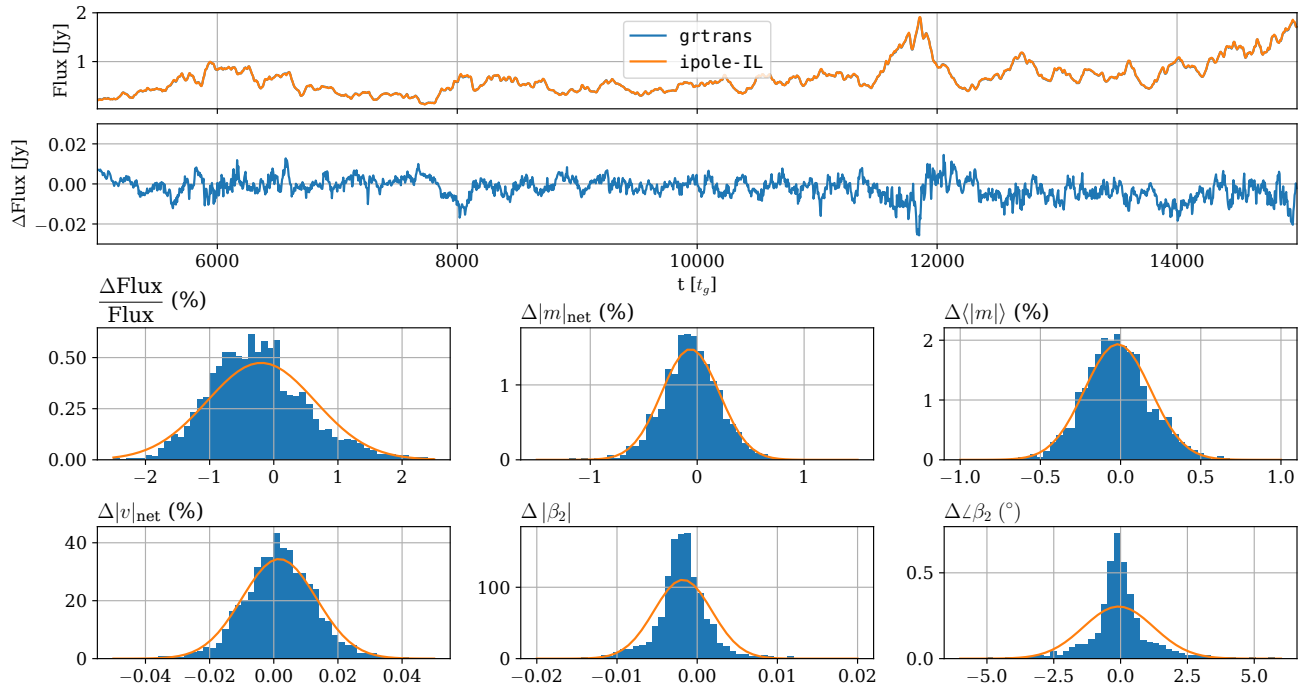


Figure 11. (upper plots) Comparison of total flux density computed by *ipole*-IL and *grtrans* over 10,000 r_g/c of a MAD GRMHD simulation. The upper plot shows the total (Stokes I) flux density produced by each code, and the lower the absolute difference in flux densities. (lower plots) Histograms comparing image metrics between corresponding images over the entire window. Each histogram is computed with a total of 50 bins across the domain shown, with any values outside the range added to the final bins.

REFERENCES

- Bronzwaer, T., Davelaar, J., Younsi, Z., et al. 2018, *A&A*, 613, A2, doi: [10.1051/0004-6361/201732149](https://doi.org/10.1051/0004-6361/201732149)
- Bronzwaer, T., Younsi, Z., Davelaar, J., & Falcke, H. 2020, *A&A*, 641, A126, doi: [10.1051/0004-6361/202038573](https://doi.org/10.1051/0004-6361/202038573)
- Chandrasekhar, S. 1960, Radiative transfer

- Davelaar, J., Bronzwaer, T., Kok, D., et al. 2018, *Computational Astrophysics and Cosmology*, 5, 1, doi: [10.1186/s40668-018-0023-7](https://doi.org/10.1186/s40668-018-0023-7)
- Davelaar, J., & Haiman, Z. 2022, *PhRvD*, 105, 103010, doi: [10.1103/PhysRevD.105.103010](https://doi.org/10.1103/PhysRevD.105.103010)
- Davelaar, J., Olivares, H., Porth, O., et al. 2019, *A&A*, 632, A2, doi: [10.1051/0004-6361/201936150](https://doi.org/10.1051/0004-6361/201936150)
- Dexter, J. 2016, *MNRAS*, 462, 115, doi: [10.1093/mnras/stw1526](https://doi.org/10.1093/mnras/stw1526)
- Dexter, J., & Agol, E. 2009, *ApJ*, 696, 1616, doi: [10.1088/0004-637X/696/2/1616](https://doi.org/10.1088/0004-637X/696/2/1616)
- Event Horizon Telescope Collaboration, Akiyama, K., Alberdi, A., et al. 2019a, *ApJL*, 875, L1, doi: [10.3847/2041-8213/ab0ec7](https://doi.org/10.3847/2041-8213/ab0ec7)
- . 2019b, *ApJL*, 875, L2, doi: [10.3847/2041-8213/ab0c96](https://doi.org/10.3847/2041-8213/ab0c96)
- . 2019c, *ApJL*, 875, L3, doi: [10.3847/2041-8213/ab0c57](https://doi.org/10.3847/2041-8213/ab0c57)
- . 2019d, *ApJL*, 875, L4, doi: [10.3847/2041-8213/ab0e85](https://doi.org/10.3847/2041-8213/ab0e85)
- . 2019e, *ApJL*, 875, L5, doi: [10.3847/2041-8213/ab0f43](https://doi.org/10.3847/2041-8213/ab0f43)
- . 2019f, *ApJL*, 875, L6, doi: [10.3847/2041-8213/ab1141](https://doi.org/10.3847/2041-8213/ab1141)
- Event Horizon Telescope Collaboration, Akiyama, K., Algaba, J. C., et al. 2021a, *ApJL*, 910, L12, doi: [10.3847/2041-8213/abe71d](https://doi.org/10.3847/2041-8213/abe71d)
- . 2021b, *ApJL*, 910, L13, doi: [10.3847/2041-8213/abe4de](https://doi.org/10.3847/2041-8213/abe4de)
- Event Horizon Telescope Collaboration, Akiyama, K., Alberdi, A., et al. 2022a, *ApJL*, 930, L12, doi: [10.3847/2041-8213/ac6674](https://doi.org/10.3847/2041-8213/ac6674)
- . 2022b, *ApJL*, 930, L13, doi: [10.3847/2041-8213/ac6675](https://doi.org/10.3847/2041-8213/ac6675)
- . 2022c, *ApJL*, 930, L14, doi: [10.3847/2041-8213/ac6429](https://doi.org/10.3847/2041-8213/ac6429)
- . 2022d, *ApJL*, 930, L15, doi: [10.3847/2041-8213/ac6736](https://doi.org/10.3847/2041-8213/ac6736)
- . 2022e, *ApJL*, 930, L16, doi: [10.3847/2041-8213/ac6672](https://doi.org/10.3847/2041-8213/ac6672)
- . 2022f, *ApJL*, 930, L17, doi: [10.3847/2041-8213/ac6756](https://doi.org/10.3847/2041-8213/ac6756)
- Gold, R., Broderick, A. E., Younsi, Z., et al. 2020, *ApJ*, 897, 148, doi: [10.3847/1538-4357/ab96c6](https://doi.org/10.3847/1538-4357/ab96c6)
- Hindmarsh, A. C. 2019, ODEPACK: Ordinary differential equation solver library, *Astrophysics Source Code Library*, record ascl:1905.021. <http://ascl.net/1905.021>
- Landi Degl'Innocenti, E., & Landi Degl'Innocenti, M. 1985, *SoPh*, 97, 239, doi: [10.1007/BF00165988](https://doi.org/10.1007/BF00165988)
- Mahadevan, R., & Quataert, E. 1997, *ApJ*, 490, 605, doi: [10.1086/304908](https://doi.org/10.1086/304908)
- Marszewski, A., Prather, B. S., Joshi, A. V., Pandya, A., & Gammie, C. F. 2021, *ApJ*, 921, 17, doi: [10.3847/1538-4357/ac1b28](https://doi.org/10.3847/1538-4357/ac1b28)
- Mościbrodzka, M. 2020, *MNRAS*, 491, 4807, doi: [10.1093/mnras/stz3329](https://doi.org/10.1093/mnras/stz3329)
- Mościbrodzka, M., Falcke, H., & Noble, S. 2016, *A&A*, 596, A13, doi: [10.1051/0004-6361/201629157](https://doi.org/10.1051/0004-6361/201629157)
- Mościbrodzka, M., & Gammie, C. F. 2018, *MNRAS*, 475, 43, doi: [10.1093/mnras/stx3162](https://doi.org/10.1093/mnras/stx3162)
- Noble, S. C., Leung, P. K., Gammie, C. F., & Book, L. G. 2007, *Classical and Quantum Gravity*, 24, S259, doi: [10.1088/0264-9381/24/12/S17](https://doi.org/10.1088/0264-9381/24/12/S17)
- Novikov, I. D., & Thorne, K. S. 1973, in *Black Holes (Les Astres Occlus)*, 343–450
- Page, D. N., & Thorne, K. S. 1974, *ApJ*, 191, 499, doi: [10.1086/152990](https://doi.org/10.1086/152990)
- Palumbo, D. C. M., Wong, G. N., & Prather, B. S. 2020, *ApJ*, 894, 156, doi: [10.3847/1538-4357/ab86ac](https://doi.org/10.3847/1538-4357/ab86ac)
- Pandya, A., Zhang, Z., Chandra, M., & Gammie, C. F. 2016, *ApJ*, 822, 34, doi: [10.3847/0004-637X/822/1/34](https://doi.org/10.3847/0004-637X/822/1/34)
- Pihajoki, P., Mannerkoski, M., Nättilä, J., & Johansson, P. H. 2018, *Arcmancer*, 0.2.0, Zenodo, Zenodo, doi: [10.5281/zenodo.1264666](https://doi.org/10.5281/zenodo.1264666)
- Pordes, R., Petravick, D., Kramer, B., et al. 2007, in 78, Vol. 78, *J. Phys. Conf. Ser.*, 012057, doi: [10.1088/1742-6596/78/1/012057](https://doi.org/10.1088/1742-6596/78/1/012057)
- Prather, B., Wong, G., Dhruv, V., et al. 2021, *The Journal of Open Source Software*, 6, 3336, doi: [10.21105/joss.03336](https://doi.org/10.21105/joss.03336)
- Pu, H.-Y., & Broderick, A. E. 2018, *ApJ*, 863, 148, doi: [10.3847/1538-4357/aad086](https://doi.org/10.3847/1538-4357/aad086)
- Pu, H.-Y., Yun, K., Younsi, Z., & Yoon, S.-J. 2016, *ApJ*, 820, 105, doi: [10.3847/0004-637X/820/2/105](https://doi.org/10.3847/0004-637X/820/2/105)
- Rees, D. E., Murphy, G. A., & Durrant, C. J. 1989, *ApJ*, 339, 1093, doi: [10.1086/167364](https://doi.org/10.1086/167364)
- Ryan, B. R., Ressler, S. M., Dolence, J. C., et al. 2017, *ApJL*, 844, L24, doi: [10.3847/2041-8213/aa8034](https://doi.org/10.3847/2041-8213/aa8034)
- Schnittman, J. D., & Krolik, J. H. 2009, *ApJ*, 701, 1175, doi: [10.1088/0004-637X/701/2/1175](https://doi.org/10.1088/0004-637X/701/2/1175)
- Sfiligoi, I., Bradley, D. C., Holzman, B., et al. 2009, in 2, Vol. 2, 2009 WRI World Congress on Computer Science and Information Engineering, 428–432, doi: [10.1109/CSIE.2009.950](https://doi.org/10.1109/CSIE.2009.950)
- Shcherbakov, R. V. 2008, *ApJ*, 688, 695, doi: [10.1086/592326](https://doi.org/10.1086/592326)
- Sądowski, A., Wielgus, M., Narayan, R., et al. 2017, *MNRAS*, 466, 705, doi: [10.1093/mnras/stw3116](https://doi.org/10.1093/mnras/stw3116)
- Wong, G. N., Prather, B. S., Dhruv, V., et al. 2022, *ApJS*, 259, 64, doi: [10.3847/1538-4365/ac582e](https://doi.org/10.3847/1538-4365/ac582e)
- Younsi, Z., Porth, O., Mizuno, Y., Fromm, C. M., & Olivares, H. 2020, in *Perseus in Sicily: From Black Hole to Cluster Outskirts*, ed. K. Asada, E. de Gouveia Dal Pino, M. Giroletti, H. Nagai, & R. Nemmen, Vol. 342, 9–12, doi: [10.1017/S1743921318007263](https://doi.org/10.1017/S1743921318007263)
- Younsi, Z., Wu, K., & Fuerst, S. V. 2012, *A&A*, 545, A13, doi: [10.1051/0004-6361/201219599](https://doi.org/10.1051/0004-6361/201219599)